Charles University in Prague
Faculty of Mathematics and Physics

BACHELOR THESIS

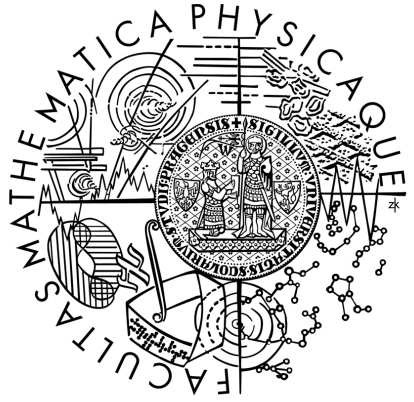

Petr Opletal

Study of magnetic quantum critical features on uranium compounds

Department of Condensed Matter Physics

Supervisor of the bachelor thesis: RNDr. Jiří Pospíšil, Ph.D.

Study programme: Physics
Specialization: General Physics

Prague 2013

Univerzita Karlova v Praze
Matematicko-fyzikální fakulta

BAKALÁŘSKÁ PRÁCE

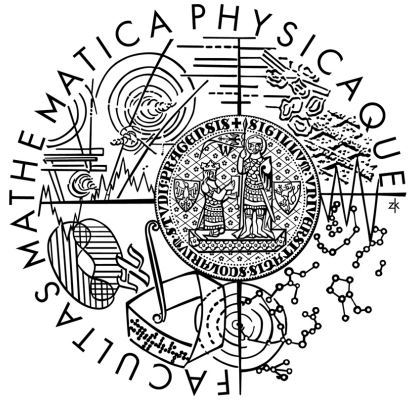

Petr Opletal

Studium magnetických kvantově kritických jevů na uranových sloučeninách

Katedra fyziky kondenzovaných látek

Vedoucí bakalářské práce: RNDr. Jiří Pospíšil, Ph.D.

Studijní program: Fyzika
Studijní obor: Obecná fyzika

Praha 2013

I would like to thank my supervisor RNDr. Jiří Pospíšil Ph.D. for his helpful support, time, advices, indispensable guide in my work and patience with me. Further I would like to thank to prof. RNDr. Vladimír Sechovský, DrSc for his valuable comments and suggestions. I sincerely thank to Bc. Michal Vališka and Ing. Barbora Vondráčková for all their help and advices in laboratories. I want also to thank to RNDr. Jiří Prchal, Ph.D. for his help with measuring in close cycle cooling system. Last but not least I want to thank to my family for all their support.

I declare that I carried out this bachelor thesis independently, and only with the cited sources, literature and other professional sources.

I understand that my work relates to the rights and obligations under the Act No. 121/2000 Coll., the Copyright Act, as amended, in particular the fact that the Charles University in Prague has the right to conclude a license agreement on the use of this work as a school work pursuant to Section 60 paragraph 1 of the Copyright Act.

In Prague date 23.5.2013 Petr Opletal

Název práce: Studium magnetických kvantově kritických jevů na uranových sloučeninách

Autor: Petr Opletal

Katedra: Katedra fyziky kondenzovaných látek

Vedoucí bakalářské práce: RNDr. Jiří Pospíšil, Ph.D., Katedra fyziky kondenzovaných látek

Abstrakt: Předmětem této práce je studium magnetického fázového diagramu pseudoternárního systému $UCo_xRu_{1-x}Al$. Czochralského metodou byly úspěšně připraveny tři různé monokrystaly o složení $UCo_{0.19}Ru_{0.81}Al$, $UCo_{0.27}Ru_{0.73}Al$ a $UCo_{0.40}Ru_{0.60}Al$. Složení bylo potvrzeno EDX analýzou a kvalita monokrystalů byla ověřena Laueho metodou. Krystalografické parametry byly stanoveny rentgenovou práškovou difrakcí. Analýza naměřených dat potvrdila silnou jednoosou magnetokrystalovou anizotropii (snadný směr magnetizace v ose c) a existenci tvrdé a měkké feromagnetické fáze. Pro $UCo_{0.40}Ru_{0.60}Al$ byla určena Curieova teplota $T_C = 41$ K a pro přechod z feromagneticky měkké fáze do feromagneticky tvrdé fáze při 35 K. $UCo_{0.27}Ru_{0.73}Al$ přechází do feromagnetického stavu (měkká fáze) při $T_C = 18$ K a měkká fáze přechází do tvrdé při teplotě okolo 7 K. Sloučenina $UCo_{0.19}Ru_{0.81}Al$ zůstává paramgnetická do 2 K. Analýza teplotní závislosti měrného tepla a elektrického odporu ukazuje na chování odlišné od Fermiho kapaliny, což souvisí s blízkostí kvantově kritického bodu.

Klíčová slova: UCoAl, URuAl, kvantově kritický bod, feromagnetismus

Title: Study of magnetic quantum critical features on uranium compounds

Author: Petr Opletal

Department: Department of Condensed Matter Physics

Supervisor: RNDr. Jiří Pospíšil, Ph.D, Department of Condensed Matter Physics

Abstract: Motivation of this thesis is a study of magnetic phase diagram of the pseudoternary system $UCo_xRu_{1-x}Al$. Three single crystals $UCo_{0.19}Ru_{0.81}Al$, $UCo_{0.27}Ru_{0.73}Al$ and $UCo_{0.40}Ru_{0.60}Al$ have been successfully prepared by Czochralski method. Composition was confirmed by EDX analysis and quality of single crystals was checked by Laue method. Crystallographic parameters and occupancies were determined by X-ray powder diffraction. Data analysis confirmed strong uniaxial magnetocrystalline anisotropy (c is the easy magnetization axis) and existence of hard and soft ferromagnetic phase. Curie temperature $T_C = 41$ K was determined for $UCo_{0.40}Ru_{0.60}Al$ and phase transition from the soft ferromagnetic phase to the hard one takes place at 35 K. $UCo_{0.27}Ru_{0.73}Al$ becomes ferromagnetic at $T_C = 18$ K and the transition from the soft to the hard ferromagnetic phase takes place somewhere around 7 K. $UCo_{0.19}Ru_{0.81}Al$ is paramagnetic down to 2 K. Analysis of the temperature dependence of resistivity and heat capacity reveals signatures of non-Fermi liquid behaviour due to proximity of quantum critical point.

Keywords: UCoAl, URuAl, quantum critical point, ferromagnetism

Contents

1. Introduction

Rare-earth intermetallics are group of intensively studied compounds in modern solid state physics. The scientific interest is given by large variety of physical features of these compounds. The unique physical phenomena observed in many rare earth intermetallic have origin in character of their *4f* electon states, which are well localized. Although all rare earth intemetallics are studied the main interest is focused on Ce and Yb compounds nowadays. Both elements are characterized by unstable valence state 3+ simple affecting by external variables. The effects like magnetism, superconductivity, even their coexistence, heavy fermion behaviour or quantum critical features are frequently observed in these materials. However, intermetallics of these elements are not only ones that are characterized by so interesting properties. Both elements have actinide counterparts which are characterized by similarly wide scale of the physical properties. One of the interesting elements among actinides is uranium and its intermetallics. Uranium intermetallics are very interesting thanks to anomalous properties of the uranium *5f* electron states. They are just on the border between the localized and itinerant character and their character can be strongly affected by external variables like applied magnetic field, pressure and chemical doping. The change of *5f* electron states leads to very interesting behaviour and phenomena which were already listed for Ce compounds.

One of the interesting group of uranium compounds are ternary intermetallics. One of these are UTX compounds, where U stands for uranium, T stands for transition metals, which are frequently from second half of *3d-* , *4d-* and 5d- series, and X stands for p-elements from IIIA, IVA and VA groups of periodic table. UTX compounds , which study is subject of this thesis can crystallize in two structural models [1]. First is orthorhombic Ti-Ni-Si type or hexagonal Zr-Ni-Al type [1]. Zr-Ni-Al type of UTX compounds are interesting for their wide range of physical features. Strong magnetocrystalline anisotropy is typical for UTX compounds of Zr-Ni-Al type [1]. It is presented in all uranium intermetallics in which *5f* elctron states contribute to magnetic moments. Extra focus was also concentrated on physical behaviour of pseudoternary systems when the evolution of physical properties was studied between two parent compounds. Such studies usually bring unexpected behaviour, where for example dome of stable magnetic state can exist between two paramagnetic neigbours. Such type of behaviour was found in many systems like $UCo_xRu_{1-x}Al$ [2], where UCoAl and URuAl are paramagnets or $UNi_xFe_{1-x}Al$ [3], where UNiAl is antiferromagnetic and UFeAl is paramagnet.

1.1 Motivation of the thesis

Motivation of my thesis is study of the phase diagram of $UCo_{1-x}Ru_xAl$ compound already mentioned in introduction. The constructed phase diagram on the basis of study of polycrystals predicts existence of two magnetic phases (Figure 1.1) [2]. The suggested phase diagram predicts that both phases should decay separately via two quantum critical points from point of view of today science with increasing Ru content. Such behaviour is unique because similar phase dia-

gram was found in UGe_2 compound, where two magnetic phases appear naturally. They are called strongly and weakly polarized ferromagnetic phase. Both can be destroyed by external pressure and quantum critical point appears. Surprisingly superconductivity originates at this region covered by ferromagnetic dome [4].

In my thesis we investigate character of magnetic phases of $UCo_xRu_{1-x}Al$ and potential presence of quantum critical point or points in $UCo_{1-x}Ru_xAl$ by measurement of thermal, magnetic and electrical properties. We estimated interesting concentrations in the $UCo_xRu_{1-x}Al$ system and grown three crystals with Co concentration x = 0.19, x = 0.27 and x = 0.40. Expected results and motivation of my work is verification of the existence of two magnetic phases in $UCo_{1-x}Ru_xAl$ system and study the structure and mechanism of decay of the expected phases.

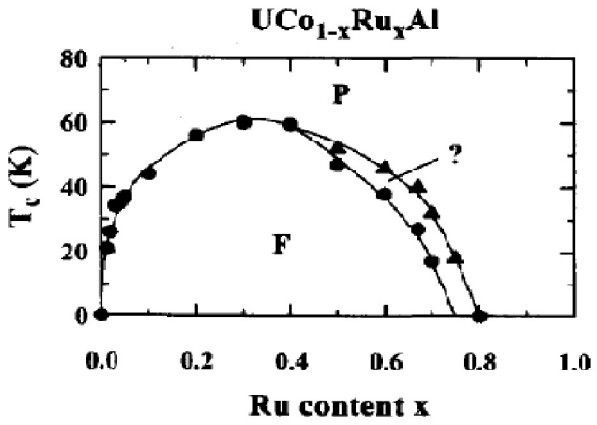

Figure 1.1: Dependence of Curie temperature T_C on concentration of Ru in $UCo_{1-x}Ru_xAl$ system [2].

1.2 Outline of the Thesis

This work has 8 chapters including this Introduction. Second part is brief theoretical overview of topics and terms used in this thesis. Next part includes description of used experimental techniques. Fourth part focuses on overview of information about UTX compounds of Zr-Ni-Al type. Results are summarized in chapter 5, which are divided in results for each crystal. Discussion of results is in Chapter 6. Final conclusions are summarized in Chapter 7 which is followed by Chapter 8 -Future plans.

2. Theory

2.1 Magnetism

Magnetism in materials is created by magnetic moments of individual ions. In classical physics a magnetic moment is represented by electric current I in a small loop of the area S. The magnetic moment is then given by:

$$\mu = IS \tag{2.1}$$

The direction of magnetic moment is normal to the area of current loop. For magnetic moments of atoms/ions, we need to find some useful unit. For that we use the mass of electron m_e and charge $-e$ orbiting in hydrogen atom. Then electrical current can be interpreted as electron circulation and we get:

$$I = \frac{-e}{T} = \frac{-ev}{2\pi r} \tag{2.2}$$

Where T is the orbital period, v is the velocity and r is the radius of the orbit. In quantum mechanics [5], we know that the angular momentum of electron ground state is:

$$m_\mathrm{e} v r = \hbar \tag{2.3}$$

From that one can get the magnetic moment of electron:

$$\mu = \pi r^2 I = -\frac{evr}{2} = -\frac{-e\hbar}{2m_\mathrm{e}} = -\mu_\mathrm{B} \quad ; \qquad \mu_\mathrm{B} = -\frac{e\hbar}{2m_\mathrm{e}} \tag{2.4}$$

where μ_B is the Bohr magneton and is used as unit of magnetic moments on atomic scale.

Solids consists of very large number of atoms with their own magnetic moments. To summarize their effects we define magnetization $\boldsymbol{M}$ as magnetic moment per unit volume. $\boldsymbol{M}$ is considered to be a vector field inside the solid. In special cases where relation between magnetization $\boldsymbol{M}$ and magnetic field $\boldsymbol{H}$ is linear we get:

$$\boldsymbol{H} = \chi \boldsymbol{M} \tag{2.5}$$

The solid in this situation is called linear material. χ is called magnetic susceptibility. Relation between magnetic induction $\boldsymbol{B}$ and $\boldsymbol{M}$ in the linear material is given by:

$$\boldsymbol{B} = \mu_0 \left(\boldsymbol{M} + \chi \boldsymbol{M}\right) = \mu_0 \left(1 + \chi\right) \boldsymbol{M} = \mu_0 \mu_\mathrm{r} \boldsymbol{M} \tag{2.6}$$

Where μ_0 is the permeability of vacuum and μ_r is the permeability of the material.

2.1.1 An atom/ion in magnetic field

Each electron in atom/ion has the spin angular moment [5] $\boldsymbol{S}$ and the orbital angular moment $\boldsymbol{L}$. The total orbital angular moment $\boldsymbol{L}$ of electrons in an atom/ion is:

$$\hbar \boldsymbol{L} = \sum_{i=1}^{Z} \boldsymbol{r_\mathrm{i}} \times \boldsymbol{p_\mathrm{i}} \tag{2.7}$$

where Z is total number of electrons in the atom/ion, r_i is the position of the i^{th} electron and p_i is its momentum. For an atom/ion we get Hamiltonian [5]:

$$\widehat{\boldsymbol{H}_0} = \sum_{i=1}^{Z} \left(\frac{p_\mathrm{i}^2}{2m_\mathrm{e}} + V_\mathrm{i} \right) \tag{2.8}$$

where $\frac{p_i^2}{2m_e}$ is the kinetic energy of the i^{th} electron and V_i is the potential energy of the i^{th} electron. Placing atom/ion into the magnetic field of induction $\boldsymbol{B}$ changes the Hamiltonian and the new Hamiltonian will be [5]:

$$\widehat{\boldsymbol{H}} = \widehat{\boldsymbol{H}_0} + \mu_\mathrm{B} \left(\boldsymbol{L} + g\boldsymbol{S} \right) \boldsymbol{B} + \frac{e^2}{8m_\mathrm{e}} \sum_{i=1}^{Z} \left(\boldsymbol{B} \times \boldsymbol{r_\mathrm{i}} \right)^2 \tag{2.9}$$

where g is the g-factor. The term $\mu_\mathrm{B} \left(\boldsymbol{L} + g\boldsymbol{S} \right) \boldsymbol{B}$ represents the atom's/ion's own magnetic moment and is called paramagnetic. The term $\frac{e^2}{8m_\mathrm{e}} \sum_{i=1}^{Z} \left(\boldsymbol{B} \times \boldsymbol{r_\mathrm{i}} \right)^2$ is known as diamagnetic moment. We can find two responses of matter on applied external magnetic field. We distinguish diamagnetic (diamagnetism) and paramagnetic (paramagnetism).

2.1.2 Diamagnetism

Diamagnetic substances have a negative susceptibility. If we apply an external magnetic field then an opposite magnetic moment is induced. Diamagnetism can be only explained by the quantum mechanics. Ignoring the paramagnetic term in equation (2.9), we get diamagnetic susceptibility defined as:

$$\chi = -\frac{Ne^2\mu_0}{V 6m_\mathrm{e}} \sum_{i=1}^{Z} \langle r_\mathrm{i}^2 \rangle \tag{2.10}$$

where N is the number of atoms/ions in the volume V. From equation (2.10) one can see that the susceptibility is negative and temperature independent. Diamagnetism is typical for atoms with full electron shells, because of zero total angular momentum.

2.1.3 Paramagnetism

Opposite of diamagnetism stands paramagnetism. An externally applied field on paramagnetic material will induce a parallel magnetization with respect to the external magnetic field. Paramgnetism can be only observed in materials containing ions with unpaired electrons. Ignoring fact that magnetic moment is quantized and can only point in some directions is called the semiclassical treatment of paramagnetism. In this approximation the paramagnetic susceptibility is given by:

$$\chi = \frac{n\mu_0\mu_\mathrm{eff}}{3k_\mathrm{B}T} = \frac{C}{T} \tag{2.11}$$

where n is the number of magnetic moments per unit volume, μ_eff is the effective magnetic moment and k_B is Boltzmann constant. The equation (2.11) is known as Curie's law (C is Curie constant characteristic for every material) and shows

that the magnetic susceptibility is positive, inversely proportional to temperature and independent on the external applied magnetic field.

It is also important to note that most of paramagnetic ions contain closed inner shells, which responds to magnetic field diamagnetically. The paramagnetic term is several orders larger than the diamagnetic one.

2.1.4 Magnetic interactions

The paramagnetic susceptibility can reach high values in low temperatures, but there is no explanation for various magnetic ordering found in many materials. The correlations between magnetic moments of ions which may yield long range magnetic ordering are mediated by magnetic interactions. Thanks to the magnetic interaction, communication among the magnetic moments is available and explain existence of a long range magnetic ordering. The most simple model considers the interaction between two electrons. From this model we obtain simple exchange Hamiltonian [5]

$$\widehat{\boldsymbol{H}} = -2J\boldsymbol{S_1}\boldsymbol{S_2} \tag{2.12}$$

where $\boldsymbol{S_1}$ and $\boldsymbol{S_2}$ are appropriate quantum numbers and J is exchange constant or exchange integral.

Phenomena of exchange interactions is important for the long range magnetic ordering. This effect is purely quantum mechanical. Model for two electrons can be generalized to a many-body system. The Hamiltonian introduced by the Heisenberg model:

$$\widehat{\mathbf{H}} = -2\sum_{i>j} J_{\mathrm{ij}}\boldsymbol{S}_{\mathbf{i}}\boldsymbol{S}_{\mathbf{j}} \tag{2.13}$$

Direct exchange: Interactions of electrons of neighbouring atoms via an exchange interaction is known as direct exchange. If wave functions of neighbouring atoms have sufficient overlap, exchange integral reaches values around 10^2 - 10^3 K and then the direct exchange can be realized. This can be found in *3d*, *4d*, *5d* and *5f* atoms/ions. Direct exchange is interaction without any intermediary and only between neighbouring atoms therefore it can be classified as short range interaction.

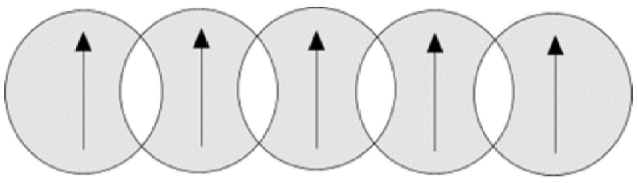

Figure 2.1: Schematic of the direct exchange interaction. Arrows represent magnetic moments.

Indirect exchange: The indirect exchange interaction (also known as superexchange) is interaction between the non-neighbouring magnetic ions mediated by a non-magnetic ion which is placed between the magnetic ions. Exchange

integral has value around 10^0 – 10^2 K. This kind of interaction can be found in compounds *3d*, *4d*, *5d*, *4f* and *5f* compounds with p and d elements.

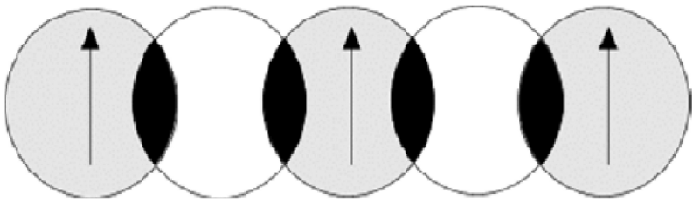

Figure 2.2: Schematic of the indirect exchange interaction. Arrows represent magnetic moments.

RKKY: In rare metals and their compounds we can find special sort of indirect exchange interaction called RKKY (after Ruderman, Kittel, Kasuya and Yosida) [6, 7, 8]. Mediators in this case are conduction electrons which interact with electrons in magnetic ions. For large $\boldsymbol{r}$ the interaction can be described by:

$$J_{\mathrm{RKKY}} \propto \frac{\cos\left(2k_{\mathrm{F}}r\right)}{r^3} \tag{2.14}$$

Where k_{F} is Fermi surface radius. Values of exchange integral can reach 10^0 – 10^2 K. This interaction long-range character which becomes effective for lanthanides, which are characterized by strongly localized *4f*-electrons excluding the direct exchange.

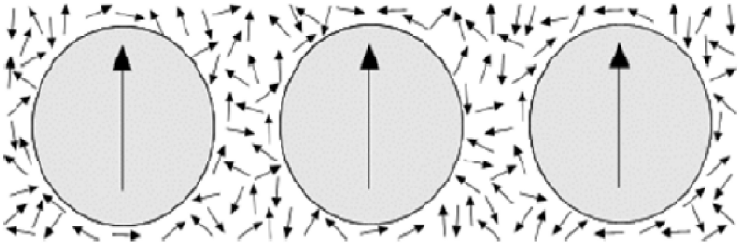

Figure 2.3: Schematic of the RKKY exchange interaction. Arrows represent magnetic moments.

2.1.5 Magnetic structures

If the energy of thermal motion is low enough and the energy of exchange interaction exceeds it then the magnetic moments spontaneously order below certain critical temperature and form a magnetic structure, a long range periodic arrangement of moments. In general the magnetic structures can be ferromagnetic and antiferromagnetic.

Ferromagnetism : In a simple ferromagnet all magnetic moments lie in one unique direction.This spontaneous magnetic ordering appears below the Curie temperature T_{C}. To describe behaviour of simple ferromagnet one can use Weiss

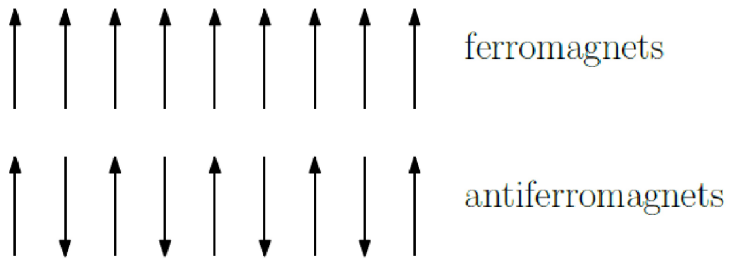

Figure 2.4: The basic types of magnetic ordering. Arrows represent magnetic moments.

model. The Weiss model approximate the action of the exchange interaction with an effective magnetic field called Weiss (molecular) field $\boldsymbol{B}_{\mathrm{mf}}$ [5]. Further, we assume that molecular field is linearly dependent on magnetization:

$$\boldsymbol{B}_{\mathrm{mf}} = \lambda \boldsymbol{M} \tag{2.15}$$

where λ is a constant which parametrizes the strength of the molecular magnetic field, it is temperature independent and positive for ferromagnets. The problem can be now treated as paramagnet placed in magnetic field $\boldsymbol{B} + \boldsymbol{B}_{\mathrm{mf}}$. The paramagnetic susceptibility will be:

$$\chi_{\mathrm{P}} = \frac{\mu_0 M}{(\boldsymbol{B} + \boldsymbol{B}_{\mathrm{eff}})} = \frac{C}{T} \tag{2.16}$$

Where C is Curie constant. If we substitute (2.15) in (2.16) we obtain:

$$\chi = \frac{M}{\mu_0 B} = \frac{C}{T - C\lambda} \tag{2.17}$$

For $T = C\lambda = T_{\mathrm{C}}$ susceptibility has singularity. At this temperature a spontaneous magnetizations emerges. From (2.17) we get Curie-Weiss law:

$$\chi = \frac{C}{T - \Theta_{\mathrm{P}}} \tag{2.18}$$

where Θ_{P} is paramagnetic Curie temperature. In Figure 2.1.5 typical dependence of magnetization and susceptibility on temperature can be seen for ferromagnets.

Antiferromagnetism: A simple antiferromagnet has antiparallel adjacent magnetic moments and the exchange integral J is negative. For antiferromagnets we get critical a temperature at which the magnetic moments order called Néel temperature T_{N}. The simple antiferromagnet can be described as system a composed of two interpenetrating sublatices where the magnetic moments of one sublattice points up and the other ones point down. The magnetic susceptibility at temperatures above T_{N} follows also Curie-Weiss law. In general we can say that Curie-Weiss law:

$$\chi = \mu_0 + \frac{C}{T - \Theta_{\mathrm{P}}} \tag{2.19}$$

represents behaviour of paramagnets, ferromagnets and antiferromagnets. Θ_{P} of simple paramagnet is zero, whereas Θ_{P} of a simple ferromagnet (antiferromagnet) is positive(negative). The paramagnetic Curie temperatures of real systems are often different from theory and therefore it needs to be treated individually.

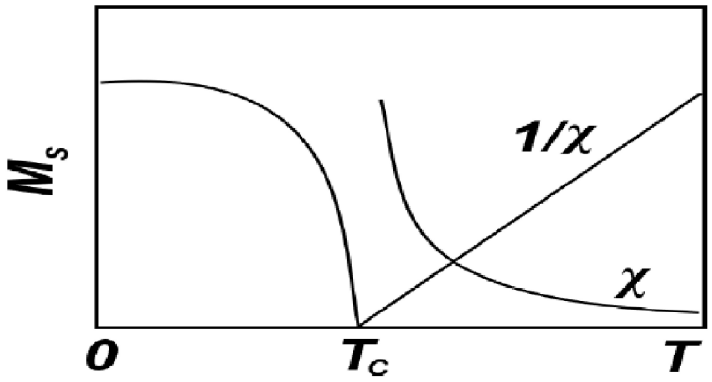

Figure 2.5: Temperature dependence of susceptibility, inverse susceptibility and the spontaneous magnetization of a ferromagnet. T_C is the Curie temperature.

2.1.6 Magnetism in *3d*, *4f* and *5f* materials and their intermetallics

***3d* magnetism – band ferromagnetism (itinerant ferromagnetism)**: In band ferromagnetism electrons near Fermi energy E_{F} from spin-down band with energy $E_{\mathrm{F}} - \Delta E$ are taken to E_{F} and their spin is flipped and placed in spin-up band where they sit with energies from E_{F} to $E_{\mathrm{F}} + \Delta E$. The number of electrons moved can be expressed as $g\left(E_{\mathrm{F}}\right)\delta E/2$ and increase in energy δE. The total change in energy is $g\left(E_{\mathrm{F}}\right)\delta E/2 \times \delta E$. The total change of kinetic energy ΔE_{KE} is:

$$\Delta E_{\mathrm{KE}} = \frac{1}{2} g\left(E_{\mathrm{F}}\right)\left(\delta E\right)^2 \tag{2.20}$$

The energy cost in form of kinetic energy is compensated by energy of interaction of magnetization with molecular field. The density of up-spins is $n_{\mathrm{u}} = \frac{1}{2}\left(n + g\left(E_{\mathrm{F}}\right)\delta E\right)$ and density of down-spins is $n_{\mathrm{d}} = \frac{1}{2}\left(n - g\left(E_{\mathrm{F}}\right)\delta E\right)$. Therefore magnetization is $M = \mu_{\mathrm{B}}\left(n_{\mathrm{u}} - n_{\mathrm{d}}\right)$, if we assume each electron has magnetic moment of 1 μ_{B}. The energy of molecular field is [5]:

$$\Delta E_{\mathrm{PE}} = -\int_0^M \mu_0 \lambda M' dM' = -\frac{1}{2}\mu_0 \lambda M^2 = -\frac{1}{2}\mu_0 \mu_{\mathrm{B}}^2 \lambda \left(n_{\mathrm{u}} - n_{\mathrm{d}}\right)^2 = -\frac{1}{2} U \left(g\left(E_{\mathrm{F}}\right)\delta E\right)^2 \tag{2.21}$$

where $U = \mu_0 \mu_{\mathrm{B}}^2 \lambda$ is measure of Coulomb energy which corresponds to molecular field which is due exchange interaction which is due coulomb energy. The total change of energy ΔE:

$$\Delta E = \Delta E_{\mathrm{KE}} + \Delta E_{\mathrm{PE}} = \frac{1}{2} g\left(E_{\mathrm{F}}\right)\left(\delta E\right)^2 \left(1 - U g\left(E_{\mathrm{F}}\right)\right) \tag{2.22}$$

The magnetic moments spontaneously align if $\Delta E < 0$ which is implies that:

$$U g\left(E_{\mathrm{F}}\right) \geq 1 \tag{2.23}$$

Which is known as Stoner criterion [5]. Large density near Fermi energy and strong Coulomb effects are required for ferromagnetic instability.

***4f* magnetism - localized magnetism**: Majority of *4f* electron density is deeply embedded inside the core of a lanthanide atoms. This leads to weak interaction with environment. This fact is documented thanks to neutron spectroscopy experiments [9] which have revealed negligible mixing of *4f* states of majority of lanthanides with conduction and valence electron states of neighbouring atoms. In band magnetism the angular moment $\boldsymbol{L}$ is very small thanks to the delocalization of *3d* states, and thus we consider only spin. In *4f* magnetism, thanks to the localized states we must consider angular moment and spin. Result of this is total angular moment $\boldsymbol{J}$, defined as $\boldsymbol{J} = \boldsymbol{L} + \boldsymbol{S}$ [5]. Observed ground magnetic states agree well with the corresponding RE^{3+} free ion values calculated within L-S coupling scheme.

***5f* magnetism**: In actinides the *5f* wave function extends more in space and interacts more with metallic environment. In actinides *5f* electron states change from localized to delocalized-like and uranium is right in the middle of this transition. Thanks to this we can observe lots of effects and they can be induced by external variables like magnetic field, doping and pressure. The *5f* electron states are delocalized in actinides because of their participation in bonding and considerable hybridization with the valence states of neighbouring atoms. This has serious consequences. The most important one is that the *5f* states form a more or less narrow *5f* band intersected by the Fermi energy E_{F} rather than discrete energy levels. Consequently, the magnetic moments due to the delocalized *5f* electrons are considerably smaller than expected for free U^{3+} or U^{4+} ion. In case of strong delocalization the *5f* electron magnetic moment disappears. The strength of the exchange interaction between corresponding *5f* moments in actinide intermetallic is much stronger than for the *4f* moments interacting only via the conduction electrons (RKKY interaction).

Hill limit Generally two one-electron mechanisms can be considered as affecting the ionic character of the *5f* states. The first one is the *5f* electron hopping due to an overlap of the *5f* wave functions with neighbouring U atoms leading to formation of the *5f* band and their delocalization. In this mechanism is the U-U spacing (the distance between centres of two nearest uranium ions) is the crucial parametr. In uranium compounds with small U-U($d_{\mathrm{U\text{-}U}}$) spacing non-magnetic, frequently superconducting ground state is found, whereas for larger $d_{\mathrm{U\text{-}U}}$ the ground state is often magnetic. The critical value for $d_{\mathrm{U\text{-}U}}$ where the character brakes is known as Hill's limit and is empirically considered to be between 340 and 360 pm. Many exceptions can be show in which the hybridization of the *5f* electron states with valence electron states of neighbouring atoms (*5f*-ligand hybridization) plays a crucial role (Figure 2.6) [1].

2.1.7 Quantum phase transition and quantum critical point

Most common phase transition, like paramagnetism to magnetic order or from a metallic state to superconducting one, occur at finite temperatures. In these transitions the macroscopic order is destroyed by thermal fluctuations for increasing temperatures. For phase transition at zero temperature, where thermal fluctuations are suppressed, a different class of phase transitions occur. Such a transition is called quantum phase transitions (QPT). It was pointed out by

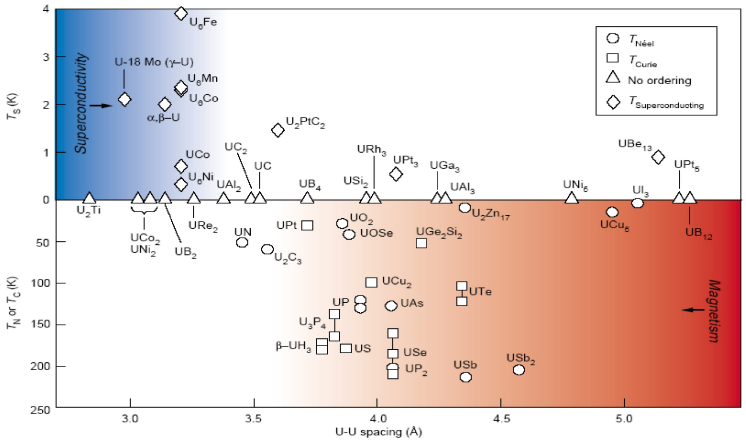

Figure 2.6: Hill's plot

Hertz [10] that when non-thermal control parameter p like pressure, magnetic field or chemical composition is varied to access the transition, then long range order is destroyed only by quantum fluctuations at certain points called quantum critical points (QCP), where $p = p_c$. Usual characteristic of QPT is a qualitative change in the system properties. Experiments and theoretical development in the last decade has made clear that presence of such QPT plays important role in unsolved problems of heavy-fermion compounds. The physical properties of the quantum fluctuations are different from the thermal fluctuations responsible for common, finite-temperature phase transitions. At the quantum critical point, the low-temperature thermodynamics is characterized by collective modes corresponding to fluctuations order parameter, rather by single-fermion excitations as in Fermi liquid. Therefore non-Fermi-liquid properties arise. The temperature dependencies strongly depends on dimensionality of the system and nature of interactions in the system. Schematics phase diagram is shown in Figure 2.7.

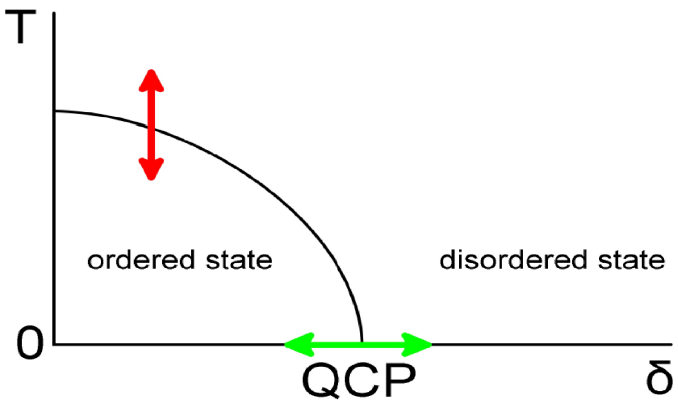

Figure 2.7: Schematic phase diagram showing ordered and disordered state. Red arrow represents classical phase transition. Quantum phase transition at zero temperature is represented by green arrow.

2.2 Heat capacity

The heat capacity (HC) represents amount of heat per unit mass of the system, required to increase its temperature by one. If it is measured in constant pressure, then it is called the isobaric heat capacity or for constant volume, then it is called the isochoric heat capacity. Whole HC is given as sum of the terms that can be expressed with equation:

$$C_{\mathrm{p}} = C_{\mathrm{ph}} + C_{\mathrm{el}} + C_{\mathrm{mag}} + C' \tag{2.24}$$

Where C_{p} is the isobaric heat capacity.

2.2.1 Electronic heat capacity C_{el}

Electronic heat capacity C_{el} represents electron contribution to the heat capacity. From classical model we have the electronic heat capacity for metals equal to 1.5 R [11], but this is true only at high temperatures. For low temperatures we have to approach problem from quantum mechanics view, where we take in account electrons as fermions obeying Fermi-Dirac statistic. Therefore only some small part of electrons states which are near the Fermi level can be excited. To calculate the value of the electron contribution to the heat capacity we must consider that the temperature increases from 0 K to T evokes the changes of internal energy:

$$\Delta U = n\left(E_{\mathrm{F}}\right) k_{\mathrm{B}}^2 T^2 \tag{2.25}$$

where $n\left(E_{\mathrm{F}}\right)$ is the density of electrons states at Fermi level. E_{F} is Fermi energy level. The electronic heat capacity is a derivation of integral energy with respect to the temperature:

$$C_{\mathrm{el}} = \frac{\partial \Delta U}{\partial T} = 2n\left(E_{\mathrm{F}}\right) k_{\mathrm{B}}^2 T = \gamma T \tag{2.26}$$

Where γ is a coefficient that represents linearity of the electronic heat capacity.

2.2.2 Phonon contribution C_{ph}

Phonon contribution C_{ph} represents the phonon contribution to a heat capacity. It dominates for high temperatures and it is realized by the thermal fluctuations of the crystal lattice. The first model for a heat capacity was done by Dulong and Petit (1819). They thought that heat capacity has constant value of $C_{\mathrm{ph}} = 3NR$. For high temperatures this model corresponds well, but for low temperatures it fails, where heat capacity decreases and reaches zero for 0 K. Einstein came with model which assumed that all atoms in a solid behave like linear quantum harmonic oscillators and vibrate independently on each other. So the heat capacity given by Einstein model is [12]:

$$C_{\mathrm{ph,E}} = 3R\left(\frac{\Theta_{\mathrm{E}}}{T}\right)^2 \frac{\exp\left(\frac{\Theta_{\mathrm{E}}}{T}\right)}{\left(\exp\left(\frac{\Theta_{\mathrm{E}}}{T}\right) - 1\right)^2} \tag{2.27}$$

Where Θ_{E} is the Einstein temperature defined by:

$$\Theta_{\mathrm{E}} = \frac{\hbar\omega_{\mathrm{E}}}{k_{\mathrm{B}}} \tag{2.28}$$

Einstein model reaches zero for 0 K and $3NR$ for high temperatures. But from experiments it was observed that the heat capacity varies as T^3 at low temperatures and not exponentially as predicted by Einstein model. Debye (1912) came with model which corresponded more to the experimental data. He realized that at low-temperature vibrations of solid can be described by acoustic branches. He calculated the distribution of frequencies that correspond to acoustic waves in isotropic continuous solid. His model describes the heat capacity with equation [12]:

$$C_{\mathrm{ph,D}} = 9R\left(\frac{T}{\Theta_{\mathrm{D}}}\right)^3 \int_0^{\frac{\Theta_{\mathrm{D}}}{T}} \frac{x^4 e^x}{\left(e^x - 1\right)^2} dx \tag{2.29}$$

Where $\Theta_{\mathrm{D}} = \frac{\hbar\omega_{\mathrm{D}}}{k_{\mathrm{B}}}$ is the Debye temperature and $x = \frac{\hbar\omega}{k_{\mathrm{B}}T}$. This model reaches zero for 0 K and $3NR$ for high temperatures and it varies like T^3 at low temperatures, which corresponds better with experimental data than the Einstein model. For better description of heat capacity we have to include anisotropic anharmonic terms in the phonon contribution [13]. We can describe the phonon spectrum with modified Debye and Einstein models for acoustic and optical branches separately. We will use equation described by C.A.Martin [14]

$$C_{\mathrm{ph}} = R\left(\sum_{i=1}^{3N-3} \frac{1}{1-\alpha_{\mathrm{i,E}}T} \frac{x_{\mathrm{i,E}}^2 \exp\left(x_{\mathrm{i,E}}\right)}{\left[\exp\left(x_{\mathrm{i,E}}\right)-1\right]^2} + \frac{9}{1-\alpha_{\mathrm{D}}T}\left(\frac{T}{\Theta_{\mathrm{D}}}\right)^3 \int_0^{\frac{\Theta_{\mathrm{D}}}{T}} \frac{x^4 e^x}{\left(e^x-1\right)^2} dx\right) \tag{2.30}$$

Where $\alpha_{i,E}$ and α_D are the anharmonic coefficients and $x_E = \frac{\Theta_E}{T}$.

2.2.3 Magnetic contribution C_{mag}

A free ion in zero external magnetic field has spherically symmetrical function of electron density. The symmetry is significantly deformed when the ion is placed inside the crystal lattice, where is surrounded by other ions and electrons. The ion is than surrounded by the electrical crystal field caused by the electrostatic interaction. The electronic crystal field has the symmetry reflecting the symmetry of crystal lattice. Presence of crystal field brings the Schottky effect that splits formerly degenerated energy levels up to $(2J+1)$ levels. J is the total angular moment of the specific ion. The magnetic contribution C_{mag} to the heat capacity is then dominated by the Schottky contribution. C_{Sch} for the compounds in paramagnetic state that can be expressed by the formula [15]

$$C_{\mathrm{Sch}} = \frac{R}{T^2}\left(\frac{\sum_{i=0}^{(2J+1)} \Delta_i^2 \exp\left(-\frac{\Delta_i}{T}\right)}{\sum_{i=0}^{(2J+1)} \exp\left(-\frac{\Delta_i}{T}\right)} - \left(\frac{\sum_{i=0}^{(2J+1)} \Delta_i^2 \exp\left(-\frac{\Delta_i}{T}\right)}{\sum_{i=0}^{(2J+1)} \exp\left(-\frac{\Delta_i}{T}\right)}\right)^2\right) \tag{2.31}$$

Where T is temperature, Δ_i is the energy gap between ground state and the i^{th} energy level. The magnetic contribution also increases entropy of whole system.

For high temperatures it gives the limit value

$$S_{\mathrm{mag}} = R \ln (2J + 1) \tag{2.32}$$

3. Experimental methods

3.1 Sample preparations

3.1.1 Preparations of polycrystalline samples

Polycrystalline samples were prepared in a monoarc furnace. Stoichiometric amount of the elements were weighted in stoichiometric composition and placed on the Cu crucible. Then the chamber of monoarc is evacuated up to $10^{-6} - 10^{-7}$ mbar with simultaneous heating of walls, crucible and also weighted elements to release the absorbed gasses on surfaces. After proper evacuation the whole chamber is filled with the high purity Ar (6N), working as a protecting atmosphere and charge carrier. The melting is realized by arc which can go up to 170 A. The sample is remelted three or four times and the sample is flipped to reach the best possible homogeneity.

3.1.2 Preparations of monocrystalline samples

Preparation single crystals takes more time than preparing the polycrystalline samples. Wide scale of method is available to prepare monocrystalline samples with different principles of crystals growth. I have used the Czochralski method.

Czochralski method

The principle of the Czochralski method is vertical pulling of the crystal from the melt on seed rod. As a seed rod can be used an inert tip of material which is not dissolved in the melt (usually tungsten rod). The best case is when already grown crystal can be used as the seed rod. Various types of furnaces exist with different heating mechanisms. I have used furnace with arc heating equipped with three symmetrically arranged arcs. Stoichiometric amounts of the elements were prepared and placed in Cu crucible. If one or even more elements exceed the vapour pressure of another elements, it must be taken into account. Possible way is weighted over stoichiometric amount of that elements to prevent loss and secure amount of element in the sample. It is also important to have homogeneous melt and to reach thermal balance. Homogeneous melt can be achieved by pre-melting of the elements into polycrystalline sample, which is then placed in the triarc furnace instead of pure non-reacted elements. Then the furnace is evacuated down to 10^{-6} mbar with simultaneous baking of the walls to desorb the bounded gases. After that, the chamber is rinsed with 6N Ar up to 0.3 bar overpressure to prevent the leaks into the chamber. Melting is started and homogeneity of the heating is secured by rotation of the Cu crucible with the melt. Seed rod (tungsten in my case) is dipped inside the melt when stabilized and then is slowly pulled up with simultaneous rotation in opposite direction to copper crucible. Czochralski method can be used only for limited number of materials. Thermal balance is critical parameter during the whole crystal growth process. If the temperature of the melt is too high the surface tension is low and the melt flattens, which leads to reduction of the crystal diameter. When the surface tension is high enough the constant diameter of the crystal is hold. Whole crystal growth is controlled by

the current in arcs, which changes the temperature and by speed of translation of the seed rod upwards (which is typically around millimetres per hour). Enough skills to work with the furnace is crucial parameter.

3.1.3 Sample annealing

Materials after preparation contain many mechanical defects and proper occupancy of the atoms is not achieved. Also mechanical strain is often presented. This is thanks to fast cooling of the materials in triarc furnace when process is finished. Samples for annealing are wrapped into tantalum foil and placed in quartz tube. The tantalum foil prevents reaction between sample and silicon from tube to contaminate the annealed sample. The tube is finally sealed up to vacuum 10^{-6} mbar with simultaneous baking of the tube up to 300 °C to desorb gasses. Parameters of the annealing treatment strongly depend on the properties of material – phase diagram, melting point.

3.2 Sample characterization methods

The characterization of samples is very important in material research. Presence of impurities significantly affects physical properties of samples. It is important in magnetic studies because ferromagnetic impurities can strongly affect the bulk properties of weakly magnetic compounds. Three methods were used for analysis of samples. Powder X-ray diffraction (XRPD) and microprobe analysis - Energy Dispersive X-ray Analysis (EDX) for finding impurities. Lau method for determination of single crystal quality and their orientation.

3.2.1 X-ray methods

X-rays are part of electromagnetic radiation spectrum. They are characterized by their typical wavelength from 0.1 nm to 10 nm. One of the conditions for diffraction on sample is that the wavelength of the X-ray must be of the same order as interatomic distances. X-rays are generated by x-rays tubes, in which electrons are accelerated by high voltage and after collision with target of anode the X-rays are emitted. Anodes are typically made from Fe, Co, Ni, Mo, Cu, Zr, W etc. For each X-ray tube we have specific spectrum of X-rays, which depends on target material and accelerating voltage. All X-ray methods work on the basis of Bragg's Law [16]:

$$2d \sin(\theta) = n\lambda \tag{3.1}$$

The integer n is the order of corresponding reflection, λ is the wavelength of the X-rays, θ is Bragg's angle which gives deviation from diffraction planes hkl distanced by d.

X-ray powder diffraction

X-ray powder diffraction is analytical X-ray method used for structural analysis of materials. It is based on the idea, that if we have numerous of little grains of the material than it must exist one that is oriented in way, that it has their plains oriented to satisfy (3.1). As result, we get diffractogram which shows

dependence of reflected intensity on diffraction angle 2Θ. We have used Bruker AXS D8 Advance X-ray diffractometer with Cu X-ray tube in Brag-Brentano geometry for measuring powder diraction (Figure 3.1). In Brag-Brentano geometry detector and X-ray tube are placed in constant distance from powder sample and their distance changes accordingly to rotation of sample about the main axis of the diffractometer. The detector rotates with double angular frequency than sample. It secures that the angle between impacted and diffracted beams is the Bragg's angle Θ for the specific plane hkl.

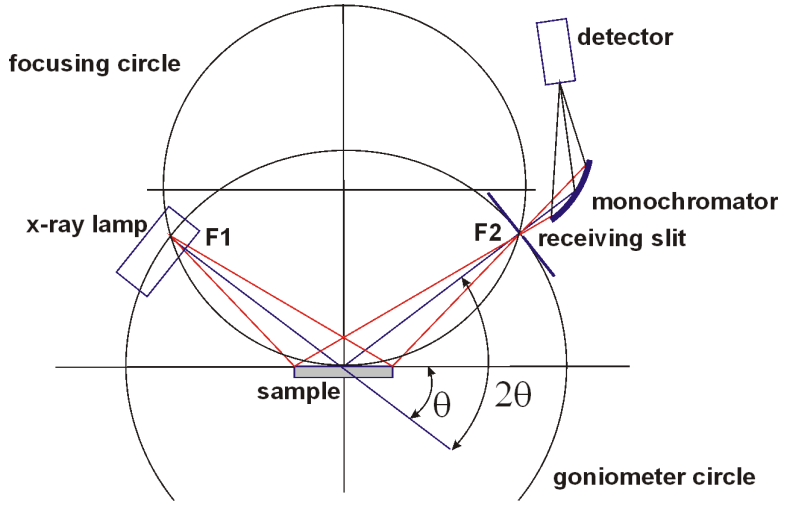

Figure 3.1: Bragg - Brentano geometry of X-ray diffractometer

Rietveld method was used for analysis of patterns. It is important to know approximate structure parameters. Diffractogram from approximate structure parameters is plotted and compared with measured diffractogram. Least square algorithm is used to match the theoretical model with measured data. The position of peaks in diffractogram depends on lattice parameters and positions of atoms. To characterize peak shaps mathematic functions like Gauss's function or Cauchy's function are used. Height of peaks depends on structural parameters. The analysis is carried out by FullProf program [17]. The analysis of lattice parameters, occupancy, and free Wyckoff positions were used to solve crystal structure of the materials.

Laue method

Laue method with back reflection geometry was used for determination of quality and orientation of our single crystals. Micrometa 600 with Cu X-ray tube with 30 kV voltage was used for measuring. Laue method works with polychromatic X-ray. In this continuous spectrum exists some wavelengths which fulfil Bragg's law. The result is image of reciprocal crystal lattice of the single crystal. The crystals are checked and oriented by placing on goniometer head and rotated to find the expected orientation. Reflection are detected on image plate join with metallic cylinder. X-ray scanner is used to read image plates. Scanned image is analysed using of LauePattern software or with Orient Express software.

Scanning electron microscope

Scanning electron microscope(SEM) is one of the types of electron microscopes. SEM Tescan Mira I LMH [18] was used, where electron beam is produced in Schottky cathode. In our microscope we use two types of detectors to produce final image: secondary electrons (SE) and backscattered electrons (BSE) detecter. BSE are based on electric scattering of electrons on material. Intensity of BSE depends on atomic number of material. Heavy elements backscatter electrons with larger intensity. This can be used to reveal tiny amounts of spurious phases and elements. Energy Dispersive X-ray Spectroscopy (EDX) is one of the analysis methods used in SEM. It is used to determine chemical composition of materials. Accelerated electrons can eject electron from its orbitals and then electron from outer shell takes its places simultaneously emitting energy in the form of x-rays. This x-rays are detected. The composition is calculated on the basis of atlas of X-ray spectra implemented in the software. The amount of the each elements is given by intensity of the spectra - characteristic lines. Bruker AXS analyzer was used with Esprit software with implemented ZAF correction.

3.3 MPMS

Magnetic Properties Measurement System made by Quantum Design and equipped with SQUID (superconducting quantum interference device) was used to measure magnetization. The sample is positioned in the center of superconducting solenoid and between SQUID detection coils. Temperature range of sample space is between 1.8 K to 400 K for MPMS. Maximum magnetic field which can be reached are 7 T created by superconducting magnet. The sensitivity of SQUID magnetometer is around 10^{-8} emu.

3.4 PPMS

Physical Properties Measurement System developed by Quantum Designs for measuring physical properties of materials in wide range of temperatures and up to magnetic field of 14 T (our device). Sample can be put in various types of inserts, specific for each measurement. Insert with sample is placed in cooling annulus which is positioned in the center of superconducting magnet. Every insert has universal connector which secures transport of measure data to computer. Special closed system with ^{3}He can be added to cool the samples down to 0.35 K. Detail of PPMS is in Figure 3.2.

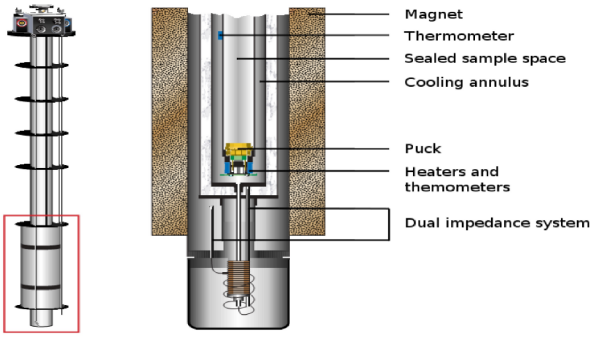

Figure 3.2: Schematic of PPMS probe and detail of lower part [19].

3.4.1 Heat capacity measurement

Heat capacity measured using PPMS equipment can be measured as function of temperature in the temperature interval 1.8 - 400 K and also with applied external magnetic field up to 14 T. The relaxation method was used. The sample must be shaped into the small plate with flat plane to have proper thermal contact with heater. Apiezon N or H (each type is used for different temperature range) are used to glue the samples to the platform. Puck for measuring heat capacity is in Figure 3.3. More details about measuring heat capacity can be found in manual [19].

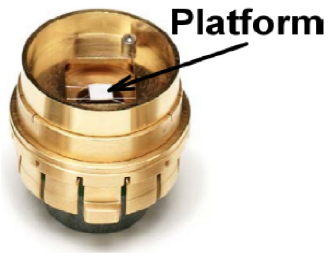

Figure 3.3: Puck for heat capacity measurements [19].

3.4.2 ACT resistivity measurements

PPMS equipment was used to measure ACT resistivity. The four terminals method was used for measurement with current of resolution of 0.02 μA and maximum value of 2 A, and voltmeter with sensitivity of 1 nV at 1 kHz. The available frequencies of the AC current range from 1 Hz to 1 kHz. The samples in the form of long beam are the best for resistivity measurement. The sample is contacted by four gold wires, where two inner contacts are connected to the voltage detector and two outer contacts are connected to current supply. Special puck for ACT is used and two samples can be measured simultaneously (Figure

3.4). The AC resistivity as function of temperature can be measured from 0.35 K to 400 K and in applied external magnetic field up to 14 T.

Figure 3.4: Puck for ACT measurements [19].

4. UTX compounds

UTX is family of compounds where T stands for transition metal atom and X for p-element from the groups IIIA, IVA and VA of the periodic table. UTX compounds can crystallize in orthorhombic Ti-Ni-Si structure, which is ordered type of $CeCu_2$ structure or in hexagonal Zr-Ni-Al structure derived from Fe_2P–type structure [1]. One of the differences between orthorhombic structure of Ti-Ni-Si type and hexagonal structure of Zr-Ni-Al type is two positions for transition metal in Zr-Ni-Al structure and one position in Ti-Ni-Si structure. The Zr-Ni-Al structure is also well defined layer system where two types layer are presented. The stacking of layers U-T1 and T2-X is typical for this structure type which is also the key to physical properties of the hexagonal UTX compounds. The layered system where many U neighbours has each uranium atom is crucial parameter for the UTX physics together with indirect interaction among UT1 layers via T2X layer. This structure system is often responsible for strong magnetocrystalline anisotropy between c and a axis. When typically the properties in the basal plane seems to be isotropic. We focus on UTX compounds which crystallize in hexagonal Zr-Ni-Al structure. Schematic view for UTX compound in Zr-Ni-Al structure are in Figure 4.1. Most of the hexagonal structures are of Zr-Ni-Al type, but there exist other hexagonal structures types like $CeIn_2$-type [1].

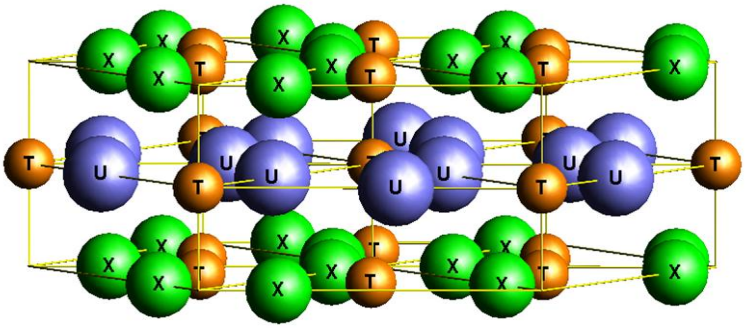

Figure 4.1: Hexagonal UTX structure of Zr-Ni-Al type. For Zr-Ni-Al structure is typical stacking of U-T and T-X planes

URuAl is paramagnetic down to 20 mK [20]. URuAl shows properties similar to spin-fluctuation system. The huge uniaxial magnetocrystalline anisotropy in paramagnetic state was found in single crystal [21, 22]. $\mu_{\mathrm{eff}} = 2.97\ \mu_{\mathrm{B}}$ was observed above 300 K from Curie-Weiss law and paramagnetic Curie temperature Θ_{P} = - 170 K and $\mu_{\mathrm{eff}} = 2.45\ \mu_{\mathrm{B}}$ was found between 100 K and 300 K and paramagnetic Curie temperature Θ_{P} = - 92 K [23]. The susceptibility is characterized by a broad maximum around 50 K. This shows that URuAl is close to magnetic ordering. The $d_{\mathrm{U\text{-}U}}$ distance is 359 pm [2].

UCoAl is paramagnetic down to low temperatures with huge magnetocrystalline anisotropy, but if we apply magnetic field about 1 T along the c-axis at temperatures below 17 K, a metamagnetic trasition is observed [24]. Heat capacity and electrical resistivity do not show any anomaly near 17 K [24]. Co atoms

does not contribute substantially to magnetism in UCoAl. Magnetic susceptibility shows broad maximum around 17 K in low magnetic fields [25]. $\mu_{\mathrm{eff}} = 1.6$ μ_{B}/U and Θ_{P} as 33 K were estimated thanks to modified Curie-Weiss law above 70 K [25]. Magnetism in UCoAl is strongly dependent on doping as shown in [26, 27, 28, 29, 2]. Ferromagnetic state can be induced by only small doping of transition metal [29, 28, 2]. UCoAl richness of phenomena is reason for studying it.

$UCo_xRu_{1-x}Al$ is pseudoternary UTX compound. Polycrystalline samples were prepared by Andreev et.al. [2]. Ferromagnetic dome was found for solution of two paramagnetic compounds. The phase diagram is shown in Figure 1.1. AC susceptibility measurements show two phase transitions of second order [2]. One from ferromagnetic state to other one for compounds with concentration x between 0.5 to 0.75.

UCoGa is characterized by huge magnetocrystalline anisotropy. It orders ferromagnetically below $T_{\mathrm{C}} = 47$ K [20, 30, 31]. Purwanto et. al. deduced magnetic moments of U atoms in ferromagnetic state of 0.74 ± 0.03 μ_{B} per atom [31]. Nakotte et. al. obtained magnetic moment in ferromagnetic state 0.74 μ_{B} per uranium atom [30]. UCoGa shows existence of two phases which is similar to $UCo_xRu_{1-x}Al$ [30].

Three typical magnetic states are found in UTX compounds of Zr-Ni-Al type and these compounds can be divided in them. All of these compounds show strong uniaxial anisotropy. Characters of these compounds are shown in Figure 4.2.

Antiferromagnetic state: UNiAl [1, 32]; UNiGa [33, 34, 1]; URhIn [35, 36]; UPdGa [37, 38].

Paramagnetic state: URuGa [1, 20].

Ferromagnetic state: UCoSn [1, 20, 39, 40, 41]; URuSb [40]; URhAl [22]; URhGa [1], URhSn [42, 41, 43].

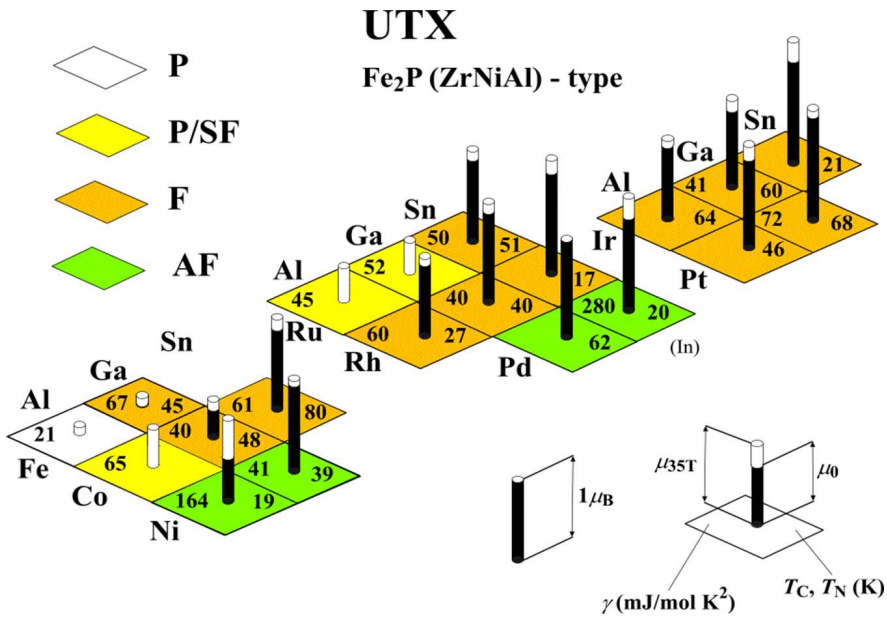

Figure 4.2: Magnetic characters of UTX compounds of Zr-Ni-Al type [1].

5. Results

5.1 Samples preparation

We have planed growth of crystals of compositions $UCo_{0.19}Ru_{0.81}Al$, $UCo_{0.27}Ru_{0.73}Al$ and $UCo_{0.40}Ru_{0.60}Al$. Polycrystalline precursors were prepared before growth of single crystals. High evaporation of Al had to be taken into account. One percent of stoichiometric amount of Al was added to compensate the evaporation. Polycrystalline precursors were melted for three times and flipped between each melting to achieve better homogeneity. The typical mass of the precursors was 11 g. Then prepared polycrystalline precursors were placed inside the triarc furnace. Single crystals have been grown by Czochralski method. Melt was heated by three symmetrically arranged arcs. Tungsten tips have been used as the seeds. The length of grown crystals was typically from 4 to 6 cm with diameter between 4 - 6 mm. The quality of all single crystals has been tested by Laue method. All single crystals were wrapped in tantalum foil, sealed in quartz tube under vacuum 10^{-6} mbar and annealed for 5 days in 900°C.

5.2 Single crystals characterization

5.2.1 Laue method

Quality of all grown crystals was verified by Laue method. It proved that grown single crystals were truly single crystals. We were also able to orient all crystals with respect to crystallographic axes using Laue method. One example of the diffractogram taken by Laue method is in Figure 5.1.

5.2.2 EDX analysis

All prepared single crystals were checked for presence of spurious phases, composition and concentration gradients. Representative images taken by SEM are summarized in Figure 5.2. No sign of the concentration gradients of the dopants has been observed. Results of the EDX analysis are in Table 5.1. Results of EDX are important for us to determine real composition of samples and resulting position in the phase diagram.

Table 5.1: Comparison between nominal concentrations in of the single crystals and concentrations obtained by EDX analysis.

Expected concentration	Concentration determined by EDX analysis
$UCo_{0.19}Ru_{0.81}Al$	$UCo_{0.22}Ru_{0.78}Al$
$UCo_{0.27}Ru_{0.73}Al$	$UCo_{0.30}Ru_{0.70}Al$
$UCo_{0.40}Ru_{0.60}Al$	$UCo_{0.44}Ru_{0.56}Al$

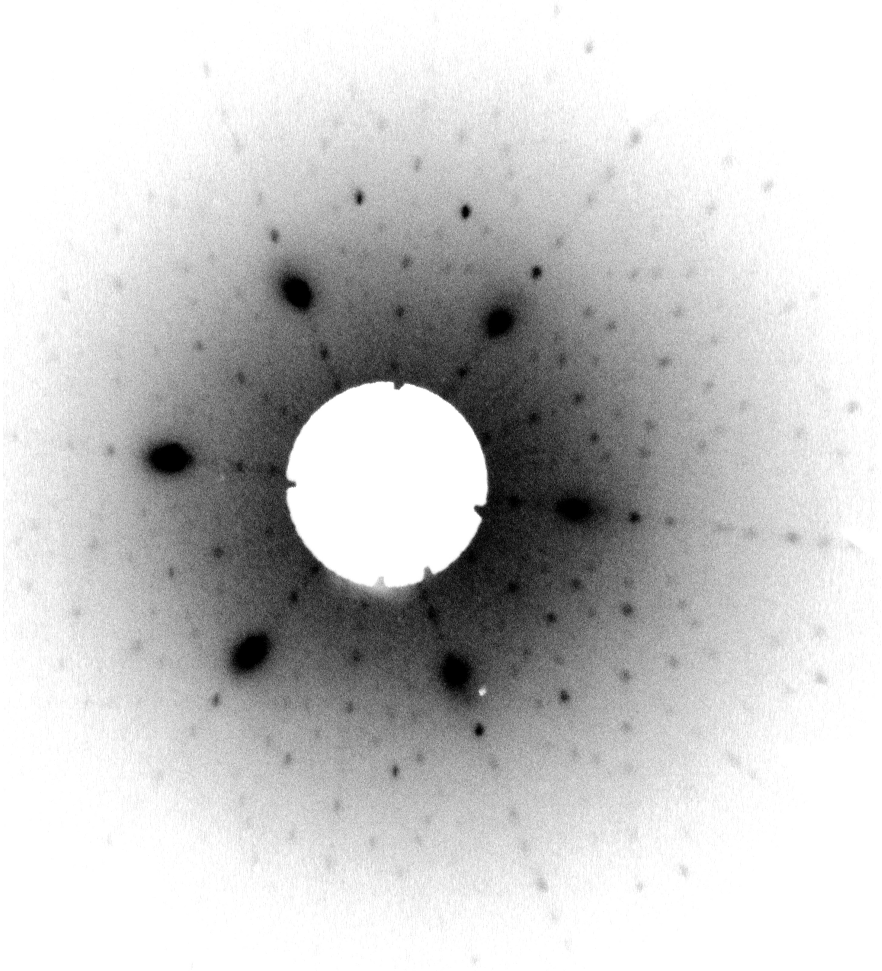

Figure 5.1: Diffractogram recorded by Laue method of the single crystal $UCo_{0.40}Ru_{0.60}Al$.

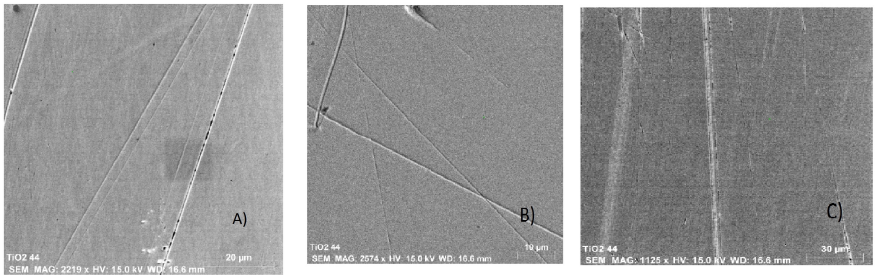

Figure 5.2: Images taken by SEM. A) shows $UCo_{0.19}Ru_{0.81}Al$, B) shows $UCo_{0.27}Ru_{0.73}Al$ and C) shows $UCo_{0.40}Ru_{0.60}Al$.

5.2.3 Reuslts of XRPD

A small part of every sample has been pulverized in the agate mortar and characterized with the XRPD. Results for all crystals are in Tables 5.2, 5.3 and 5.4. Lattice parameters as a function of concentration are shown in Figure 5.4. With increasing concentration of cobalt lattice parameters tend to be smaller. Example of diffractogram and fitted model is in Figure 5.3. It is very important to determine occupancy, because of two positions for transition metal are presented in the Zr-Ni-Al structure and preferential occupancy of *1b* is expected [3]. Evaluation of our data by Reitveld method shows different result, when position *2c* is preferably occupied by Ru (Table 5.4). However we have suggested the preferential occupancy of Ru for all single crystals. The verification of the models by single crystal diffraction is highly desirable.

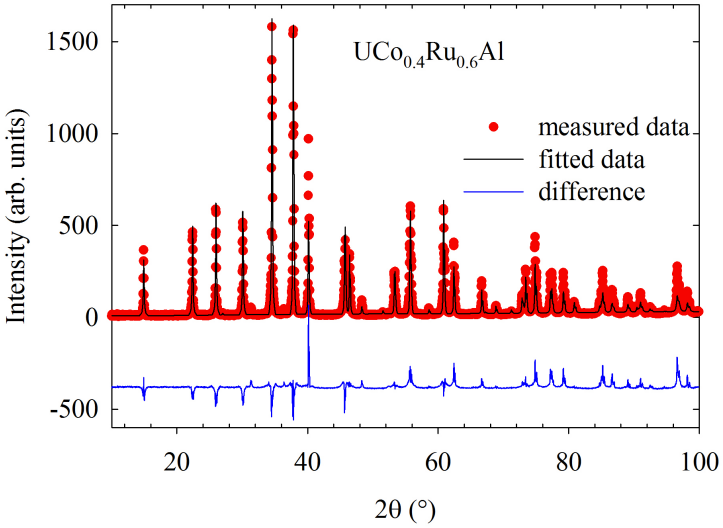

Figure 5.3: Measured and analysed data from XRPD for $UCo_{0.40}Ru_{0.60}Al$.

Table 5.2: Lattice parameters as determined by XRPD evaluation.

Co [%]	40	27	19
a [Å]	6.858	6.870	6.880
c [Å]	3.970	3.981	3.997
V [Å^3]	161.20	162.72	163.85

Table 5.3: Position of atoms with open parameters on positions U - *3g* and Al - *3f* determined by XRPD evaluation.

Co [%]	40	27	19
x of U theoretical	560	560	560
x of U analysed	581.17	583.72	582.83
x of Al theoretical	250	250	250
x of Al analysed	216.05	177.27	205.85

Table 5.4: Occupancy of atom position as given by XRPD evaluation.

Co [%]	40	27	19
Ru *1b* pos. predicted	0.05	0.0608	0.0675
Ru *1b* pos. analysed	0.0321	0.0316	0.0539
Ru *2c* pos. predicted	0.1	0.1217	0.135
Ru *2c* pos. analysed	0.1179	0.1509	0.1459
Co *1b* pos. predicted	0.0334	0.0225	0.0158
Co *1b* pos. analysed	0.0512	0.0571	0.0294
Co *2c* pos. predicted	0.0667	0.045	0.0316
Co *2c* pos. analysed	0.0487	0.0158	0.0294

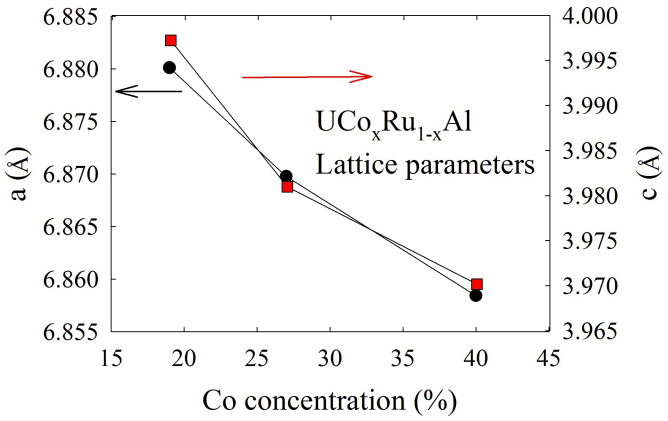

Figure 5.4: Dependence of lattice parameters on concentration of Co in $UCo_xRu_{1-x}Al$.

5.3 $UCo_{0.40}Ru_{0.60}Al$ single crystal study

We expected to find two magnetic phases on the basis of phase diagram (Figure 1.1) - magnetically soft one and hard one. The phase transition from paramagnetic state to ferromagnetic soft one should manifest around 45 K. The phase transition from soft one to hard one should be around 38 K.

5.3.1 Magnetization measurements

Magnetization measurements have been done on sample of small block shape with approximate size $1\times1\times5$ mm^3, when rectangulars planes were oriented along a and c crystallographic axis. Both DC and AC magnetization measurements were done on same sample with respect to both crystallographic orientations. We measured hysteresis loop at 4.5 K (Figure 5.5). Hysteresis loop for external magnetic field applied along c-axis shows ferromagnetic behaviour with almost rectangular shape. The value of hysteresis is about 0.5 - 0.6 T. We have determined saturated magnetic moment of 0.44 μ_B/f.u. in magnetic field of 5 T applied along the c-axis at temperature 4.5 K. Hysteresis loop for external magnetic field applied along the a-axis shows paramagnetic behaviour, which confirms strongly uniaxial behaviour and c-axis as easy magnetization axis.

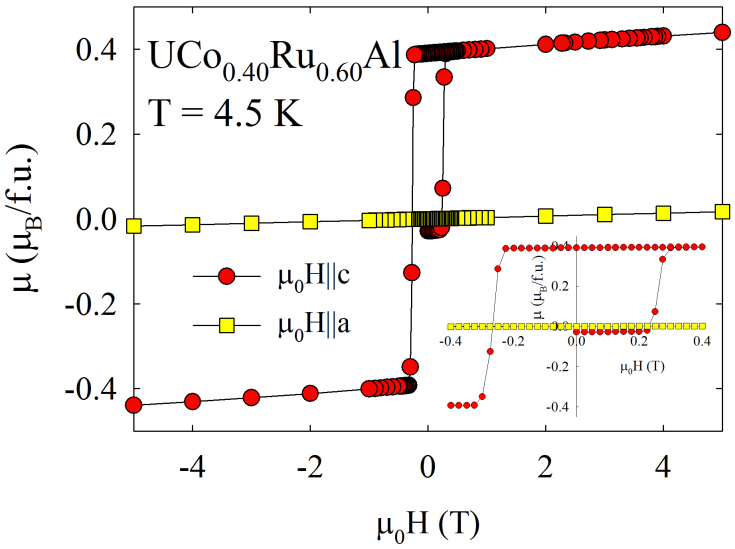

Figure 5.5: Hysteresis loop of $UCo_{0.4}Ru_{0.6}Al$ compound for external magnetic field applied along the c-axis and a-axis in 4.5 K.

The temperature dependence of AC magnetic susceptibility was measured in temperature range from 10 to 70 K, because we expect phase transitions in this range on the basis of phase diagram. Real part of AC susceptibility has maximum value at 37 K, which moves slowly to higher temperatures with higher frequencies (Figure 5.6). Imaginary part of AC susceptibility has maximum value at temperature 36 K, which moves to higher temperatures with higher frequencies as well (Figure 5.6). Imaginary part of AC susceptibility also shows sign of anomaly around 41 K in Figure 5.6. This effect is probably also in real part of AC susceptibility, but it is not so well visible. Existence both effects suggests existence of the expected phase transitions. No sign of anomaly has been found for AC susceptibility measured along the a-axis.

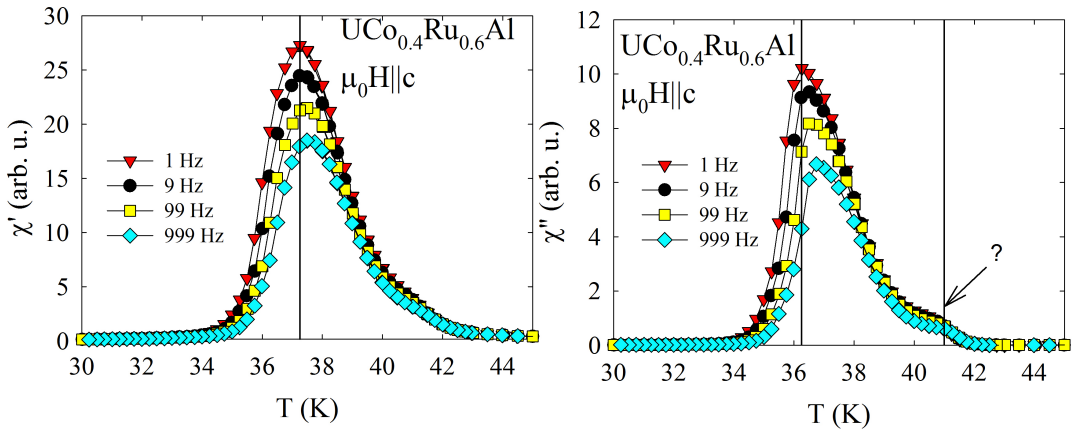

Figure 5.6: Real and imaginary part of AC susceptibility at different frequencies of $UCo_{0.4}Ru_{0.6}Al$ compound for AC magnetic field applied along the c-axis.

Measurement of temperature dependence of magnetization has been done in various external magnetic fields applied along both c-axis and a-axis. Magnetization along c-axis shows strong increase of magnetization at temperature 40 K (Figure 5.7). Nevertheless two phase transition were found. The first transition from paramagnetic state to ferromagnetic one is at $T_C = 41$ K. The second one at 35.5 K. Spontaneous magnetic moment was determined at 4.5 K and external magnetic field of 0.01 T as $\mu_{spont} = 0.39\ \mu_B$. Spontaneous magnetic moment along a-axis determined on 4.5 K and 0.01 T as μ_{spont} =1.4 $m\mu_B$ is 279 times smaller than spontaneous moment along c-axis. This confirms uniaxial anisotropy.

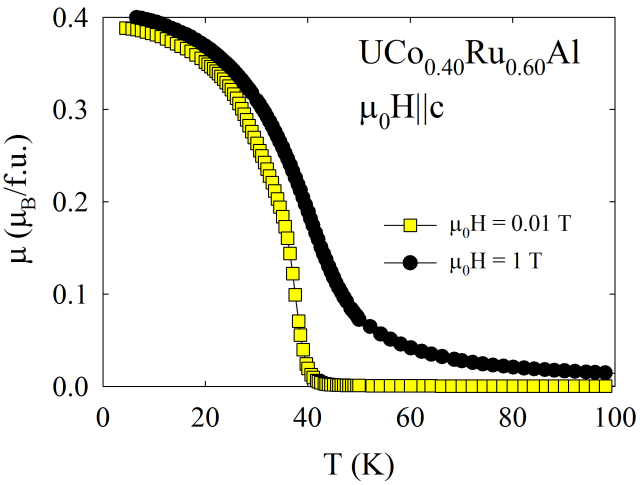

Figure 5.7: Temperature dependence of magnetization of $UCo_{0.4}Ru_{0.6}Al$ compound measured in various external magnetic field applied along the c-axis.

We have also plotted reciprocal susceptibility as a function of the temperature in various magnetic fields - see Figure 5.8. The nonlinear behaviour was found. Paramagnetic part of the data can be well evaluated by Curie Wiess law (2.19) with parameters $\Theta_P = 42.6$ K, $\mu_0 = 1.15 \cdot 10^{-8} m^3 \cdot mol^{-1}$ and effective magnetic moment of uranium $\mu_{eff} = 1.78\ \mu_B$.

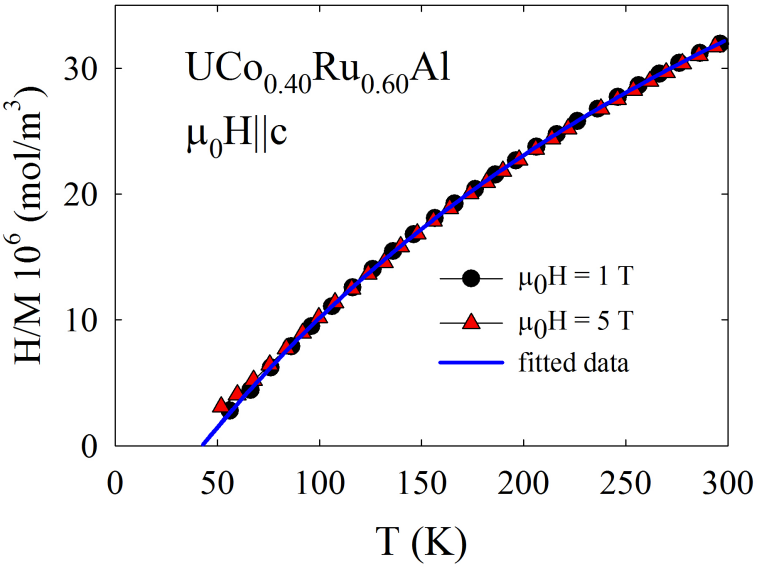

Figure 5.8: Temperature dependence of inverse susceptibility of $UCo_{0.4}Ru_{0.6}Al$ compound in various external magnetic fields applied along the c-axis.

The found anomalies in temperature dependence of magnetization and AC susceptibility motivated us to measure the set of hysteresis loops in the critical interval between 20 - 42 K in detail with fine temperature steps. Hysteresis loops at different temperatures are shown in Figure 5.9. Hysteresis loop at 20 K is characterized by shape typical for hard ferromagnet (almost rectangular shape). This trend is kept up to 30 K. Additional increase of temperature leads to change of shape of the loops to shape typical for soft ferromagnets with S-shape. The loops above 42 K have paramagnetic shape.

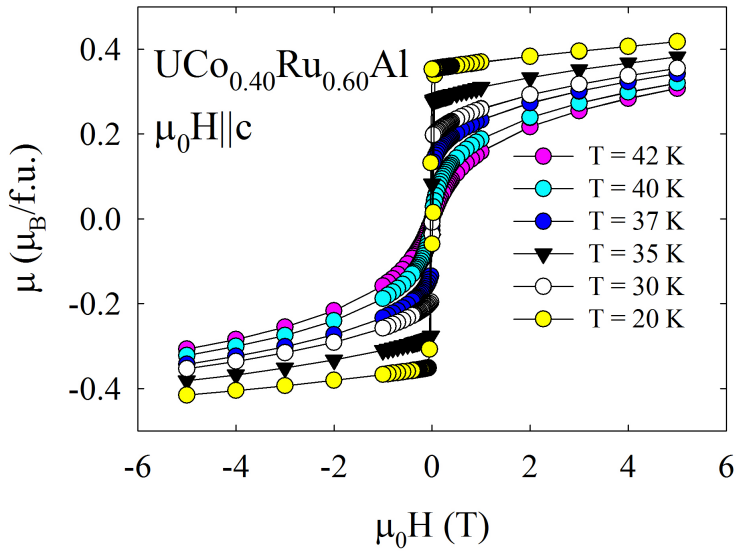

Figure 5.9: Hysteresis loops of $UCo_{0.4}Ru_{0.6}Al$ compound measured at various temperatures.

The measured hysteresis loops were also used for estimation of the Curie temperature construction of the Arrott plot [44]. Magnetization curves were measured near predicted critical temperature. Obtained Arrott plot is shown in Figure 5.10. The Curie temperature was obtained by linear fit for data in different temperatures. The resulted Curie temperature is $T_C = 39.7$ K

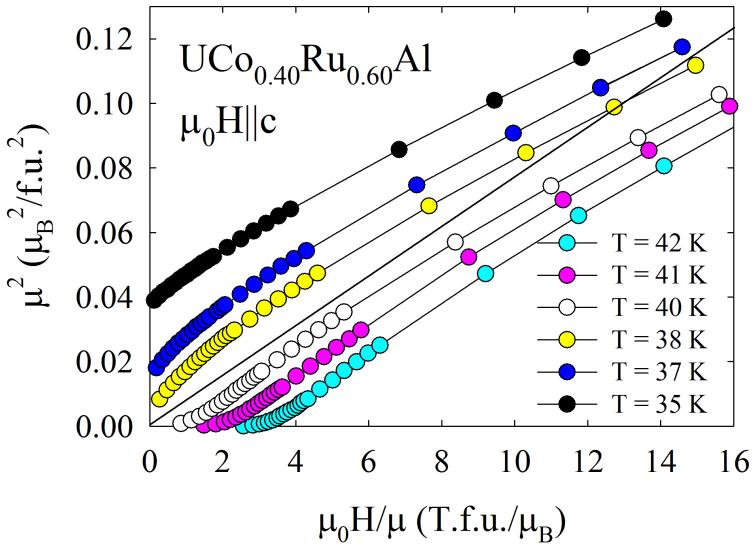

Figure 5.10: Arrott plot of $UCo_{0.4}Ru_{0.6}Al$ compound in various external magnetic fields applied along the c-axis.

5.3.2 Resistivity measurements

Resistivity measurement (ACT measurement) has been done using four probe method. The measured sample had shape of block and approximate dimension of $1\times1\times5$ mm^3 and it is the same which was used for magnetization measurement. Resistivity was measured for current applied along the c-axis and a-axis. Resistivity along the c-axis was also measured in external magnetic fields of 1 and 5 T in longitudinal arrangement. The resistivity data measured along the c-axis shows significant anomaly at 41 K (Figure 5.11). The observed anomaly starts to smear in applied magnetic field of 1 T (Figure 5.12). When we have studied the data in detail we could observe weak deviation of the trend below major anomaly. The weak effect is well visible on first derivative of data at temperature T = 35 K which can sign cross between the magnetically soft phase and hard one as expected in this crystal. The drop of resistivity has T^2 character below 35 K, when trend above this temperature is affected by already mentioned second weak anomaly. Low temperature dependence of resistivity measured along the a-axis has a metallic-like character with continuous drop.

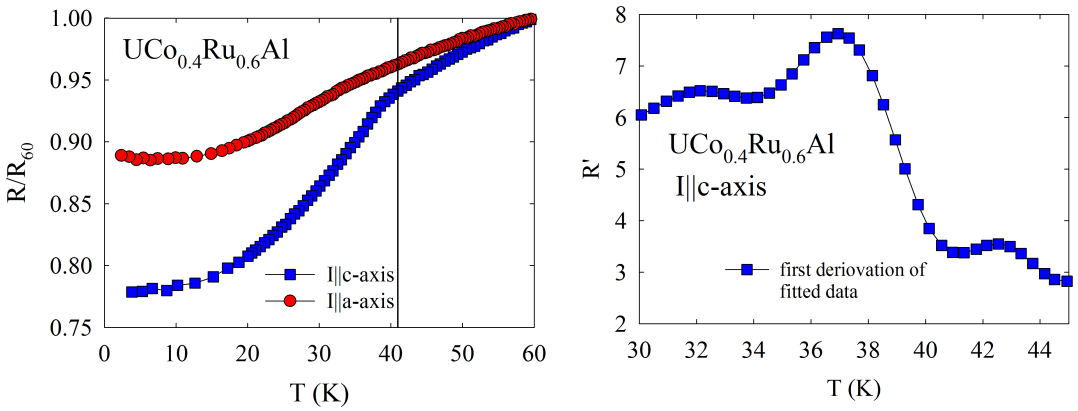

Figure 5.11: Temperature dependence of the electrical resistivity for $UCo_{0.4}Ru_{0.6}Al$ compound for current applied along the a-axis and c-axis on left and first derivation of the polynomial fit of measured resistivity data for current applied along the c-axis on right.

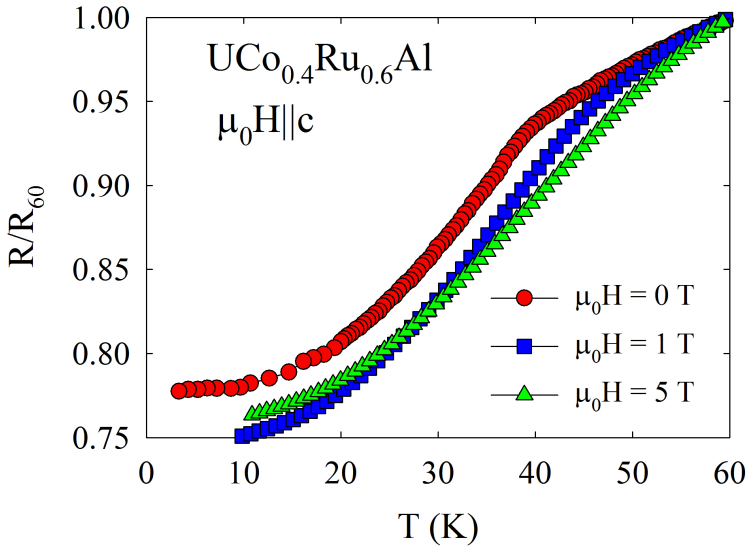

Figure 5.12: Temperature dependence of electrical resistivity for $UCo_{0.4}Ru_{0.6}Al$ compound for current applied along the c-axis in different external magnetic fields in longitudinal arrangement.

5.3.3 Heat capacity measurements

We have measured heat capacity on sample of mass of 3.09 mg in zero external magnetic field and in external magnetic field of 1 T applied along the c-axis. We show only data from 4 K to 100 K in Figure 5.13 for better clarity, because we did not find any effects in higher temperatures. We have detected weak anomaly at temperature 34.5 K in zero magnetic field. This transition becomes broaden (almost disappear) with applied magnetic field. We used Debye model for analysis of the heat capacity from 4.2 K to 50 K (Figure 5.14). Then we could

also evaluate magnetic part of heat capacity. Resulted Debye temperature was $\Theta_D = 189.7$ K. Coefficient γ was determined $\gamma = 50.3$ mJ/mol $\cdot$ K^2.

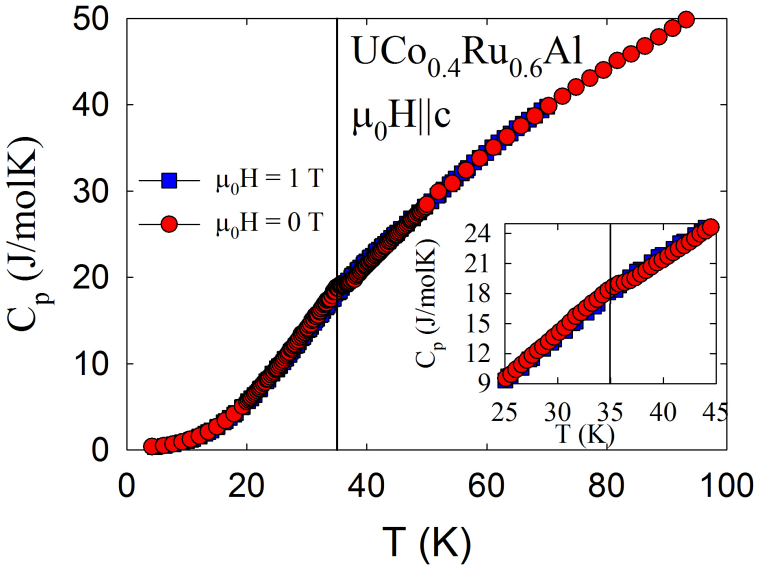

Figure 5.13: Temperature dependency of heat capacity of $UCo_{0.4}Ru_{0.6}Al$ compound.

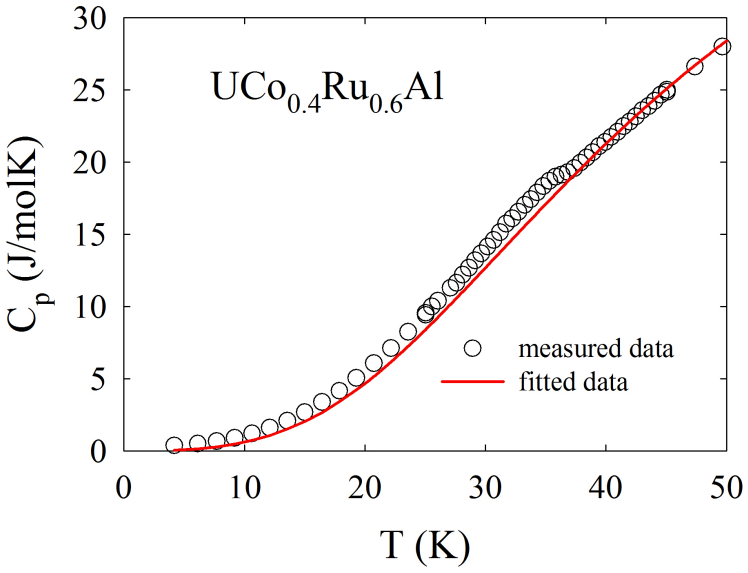

Figure 5.14: Measured data and Debye model of heat capacity of $UCo_{0.4}Ru_{0.6}Al$ compound.

5.4 $UCo_{0.27}Ru_{0.73}Al$ single crystal study

We expected to find only magnetically soft phase with respect to the phase diagram in Figure 1.1. Phase transition should manifest around 20 K.

5.4.1 Magnetization measurements

Magnetization measurements have been done on sample similar to sample of $UCo_{0.40}Ru_{0.60}Al$ compound.

We measured hysteresis loops in 1.8 K for external magnetic field applied along the a-axis and c-axis. Hysteresis loops in Figure 5.15 shows ferromagnetic behaviour for external magnetic field applied along the c-axis and paramagnetic behaviour along the a-axis, which confirms strongly uniaxial behaviour when the c-axis is easy magnetization axis. The value of hysteresis is 0.35 T. Shape of the loop stands between hard ferromagnetic (almost rectangular) and soft ferromagnetic (S-shape). Saturated magnetic moment was determined at 1.8 K in external magnetic field of 7 T as 0.32 μ_B/f.u..

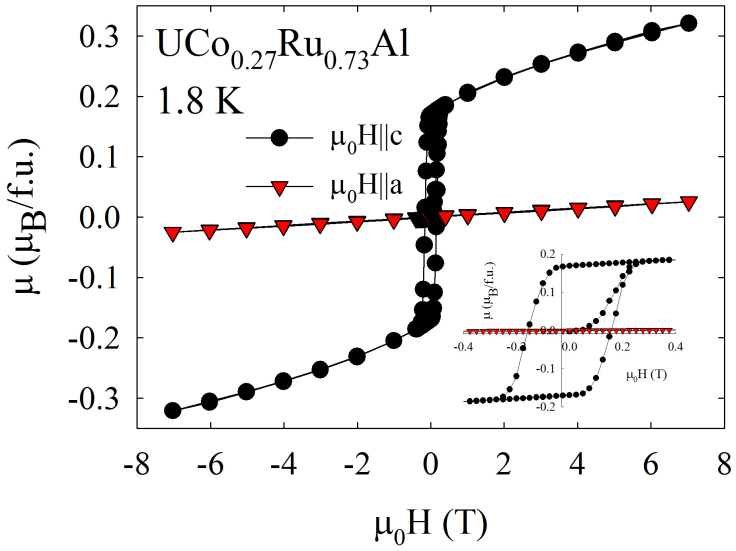

Figure 5.15: Hysteresis loop of $UCo_{0.27}Ru_{0.73}Al$ compound for external magnetic field applied along the c-axis and a-axis in 1.8 K.

Temperature dependence of the magnetization was measured by the same way as for $UCo_{0.40}Ru_{0.60}Al$ compound (Figure 5.16). One phase transition from paramagnetic phase to soft ferromagnetic one was found. Determined value of the Curie temperature is $T_C = 18.7$ K. Spontaneous magnetic moment was determined at 4.5 K in external magnetic field of 0.01 T as $\mu_{spon} = 0.15\ \mu_B$. Spontaneous magnetic moment for measuring along the a-axis was determined at 4.5 K in external magnetic field of 0.01 T as $\mu_{spont} = 0.11\ m\mu_B$ and it is 1364 times smaller than spontaneous magnetic moments along the c-axis, which confirms strong uniaxial anisotropy.

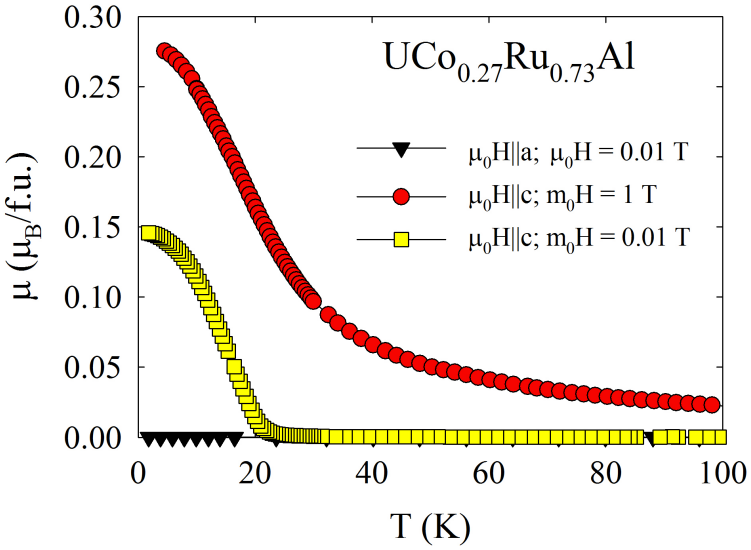

Figure 5.16: Temperature dependence of magnetization of $UCo_{0.27}Ru_{0.73}Al$ compound in various external magnetic field along the c-axis and a-axis.

Reciprocal magnetic susceptibility was evaluated and plotted by the same way as for $UCo_{0.40}Ru_{0.60}Al$ compound (Figure 5.17). The nonlinear behaviour was found. The parameters are $\mu_0 = 1.89 \cdot 10^{-8} \mathrm{m}^3 \cdot \mathrm{mol}^{-1}$, paramagnetic Curie temperature $\Theta_\mathrm{P} = 19.1$ K and effective moment of uranium $\mu_\mathrm{eff} = 2.67\ \mu_\mathrm{B}$.

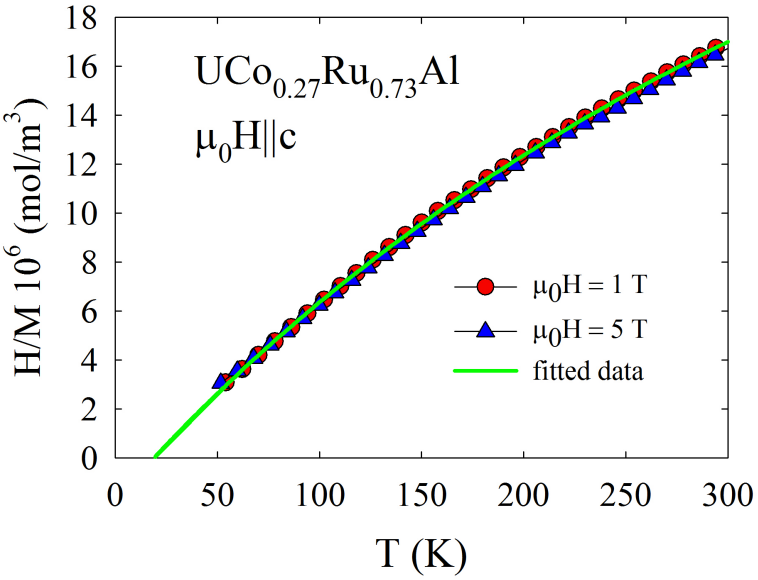

Figure 5.17: Temperature dependence of inverse susceptibility of $UCo_{0.27}Ru_{0.73}Al$ compound in various external magnetic field applied along the c-axis.

Temperature dependence of AC susceptibility was measured in temperature interval 1.8 K to 50 K, because of expected phase transition on the basis of phase diagram. Real part of AC susceptibility has maximum at 17.5 K and imaginary

part at 16.5 K, respectively. Both temperatures move to higher temperatures with higher frequencies. Measured data are shown in Figure 5.18. The width of anomaly of AC susceptibility suggests existence of phase transition below 10 K. No sign of anomaly has been found for AC susceptibility measured along the a-axis.

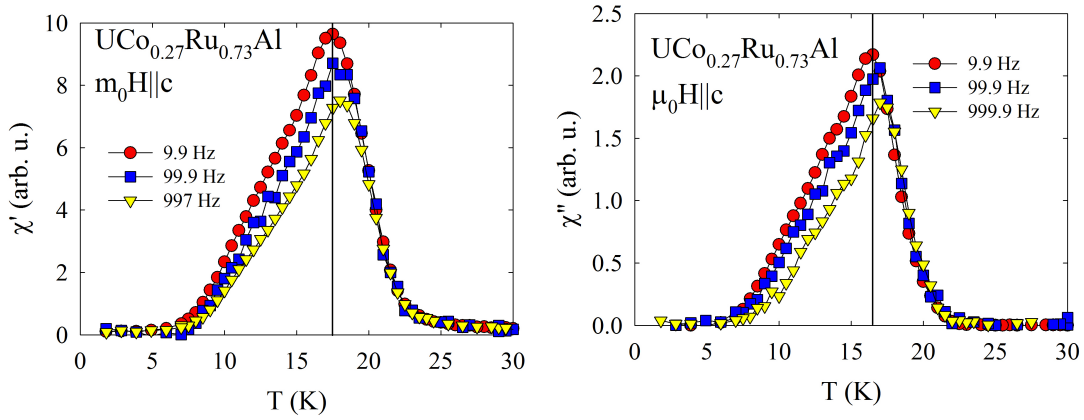

Figure 5.18: Temperature dependence of AC susceptibility of $UCo_{0.27}Ru_{0.73}Al$ compound for various frequencies of AC magnetic field applied along the c-axis.

Similar reason as in the case of $UCo_{0.40}Ru_{0.60}Al$ compound motivated us to measure the set of hysteresis loops around critical interval between 10 - 25 K in detail with fine temperature steps. Hysteresis loops at different temperatures are shown in Figure 5.19. Hysteresis loop at 10 K is characterized by shape typical for soft ferromagnet (S-shape). This trend is kept up to 25 K. Additional increase of temperature leads to change of shape of loops to shape typical for paramagnets. The loops above (including) 25 K have paramagnetic shape.

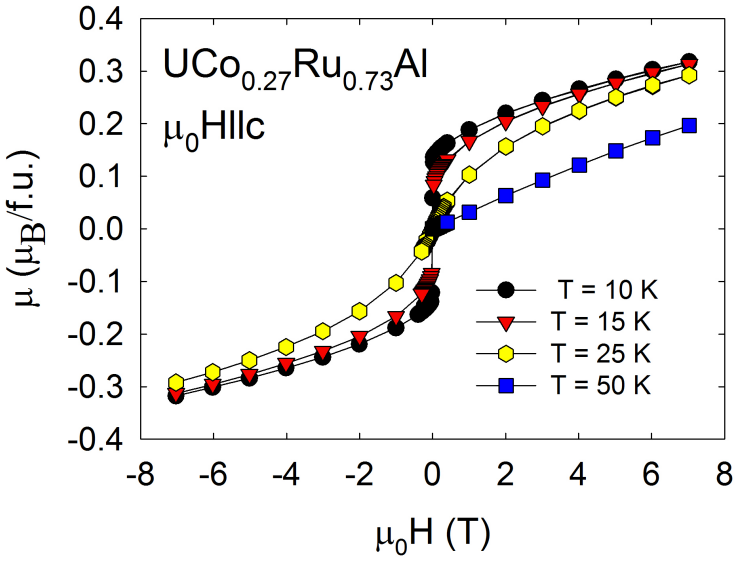

Figure 5.19: Hysteresis loops in different temperatures of $UCo_{0.27}Ru_{0.73}Al$ compound for external magnetic field applied along the c-axis.

Curie temperature $T_C = 17.2$ K was calculated using Arrott plot - see Figure 5.20.

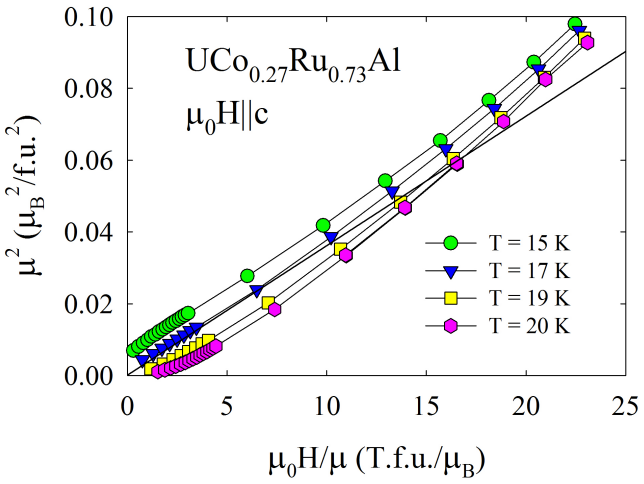

Figure 5.20: Arrott plot of $UCo_{0.27}Ru_{0.73}Al$ compound at various temperatures.

5.4.2 Resistivity measurements

Samples from magnetization measurement were used for resistivity measurement.

Electrical resistivity was measured for current applied along the c-axis and a-axis. Electrical resistivity was also measured for applied current along the c-axis in various external magnetic fields in longitudinal arrangement. The resistivity for current applied along the a-axis shows metallic behaviour and slight upturn in low temperatures (Figure 5.21). The explanation for the behaviour can be projection of the c-axis or bad contacts. We plan to re-measure the data. Determined resistivity at 300 K for current applied along the a-axis is $\rho = 5.17\ 10^{-4}\ \Omega \cdot \mathrm{m}$. The resistivity measured along the c-axis shows unusual behaviour around 19 K, when it starts to grow with lowering temperature. This effect can be suppressed by magnetic fields and disappears between magnetic field of 8 and 11 T as shown in Figure 5.22. Disappearance of resistivity growth in magnetic field suggests magnetic origin than structural one. Now we do not have any reasonable model to describe such type of behaviour in detail.

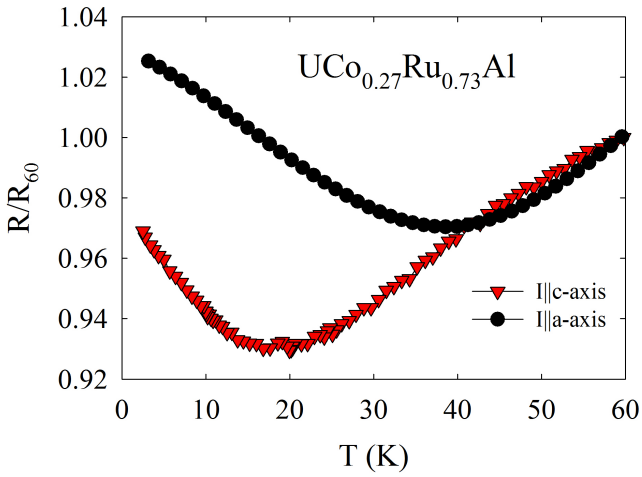

Figure 5.21: Temperature dependence of electrical resistivity $UCo_{0.27}Ru_{073}Al$ for current applied along the c-axis and a-axis.

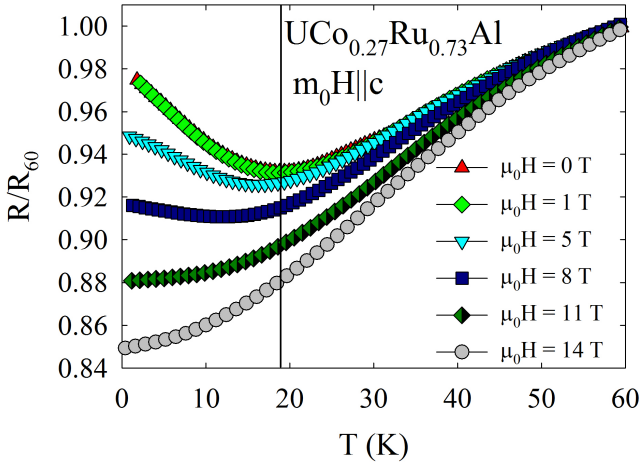

Figure 5.22: Temperature dependence of electrical resistivity $UCo_{0.27}Ru_{073}Al$ for current along the c-axis in different external magnetic fields in longitudinal arrangement.

5.4.3 Heat capacity measurements

The mass of used sample was 8.27 mg. Heat capacity was measured in zero magnetic field and in magnetic field of 14 T applied along the c-axis. Measured heat capacity is displayed in Figure 5.23. Heat capacity data shows no sign of phase transition and in addition to even magnetic field up to 14 T applied along the c-axis does not affect heat capacity in any observable way. We have evaluated magnetic part of heat capacity C_{mag} using Debye model for $UCo_{0.4}Ru_{0.6}Al$ in low temperatures. Temperature dependence of magnetic part of heat capacity divided by temperature is shown in Figure 6.8. We can see kind of linear behaviour which can sign presence of non-Fermi liquid behaviour. We had determined coefficient $\gamma = 69.4\ \mathrm{mJ/mol \cdot K^2}$. Data are shown elsewhere.

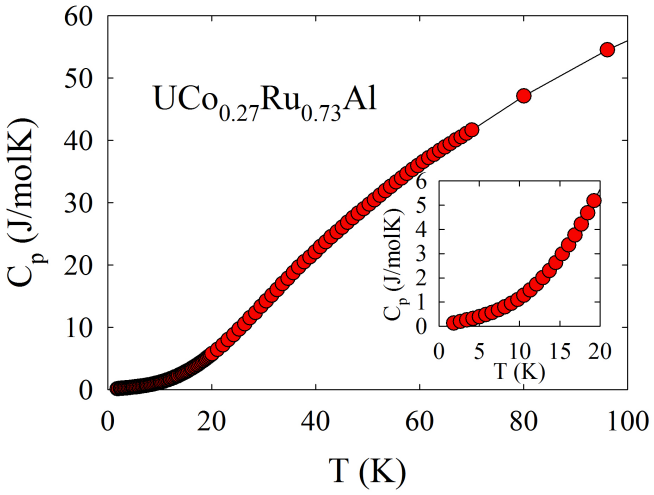

Figure 5.23: Temperature dependency of heat capacity of $UCo_{0.27}Ru_{0.73}Al$ compound. Only zero field data are shown.

5.5 $UCo_{0.19}Ru_{0.81}Al$ single crystal study

In this study we expected to find only paramagnetic phase with respect to phase diagram in Figure 1.1.

5.5.1 Magnetization measurements

Magnetization measurements has been done in similar way as for two previous ones. The strong magnetocrystalline anisotropy is conserved when the c-axis still has character of the easy magnetization axis (Figure 5.24).

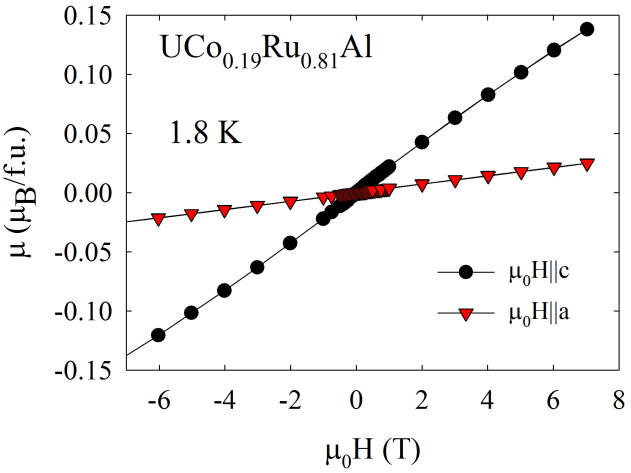

Figure 5.24: Hysteresis loops of $UCo_{0.19}Ru_{0.81}Al$ compound at temperature 1.8 K for magnetic fields applied along the c-axis and a-axis.

Reciprocal susceptibility was evaluated and plotted by the way as for $UCo_{0.40}Ru_{0.60}Al$

(Figure 5.25). Parameters of fit were $\mu_0 = 1.03 \cdot 10^{-8} \mathrm{m}^3 \cdot \mathrm{mol}^{-1}$, paramagnetic Curie temperature $\Theta_\mathrm{P} = 1.2$ K and effective moment of uranium $\mu_\mathrm{eff} = 2.03\ \mu_\mathrm{B}$.

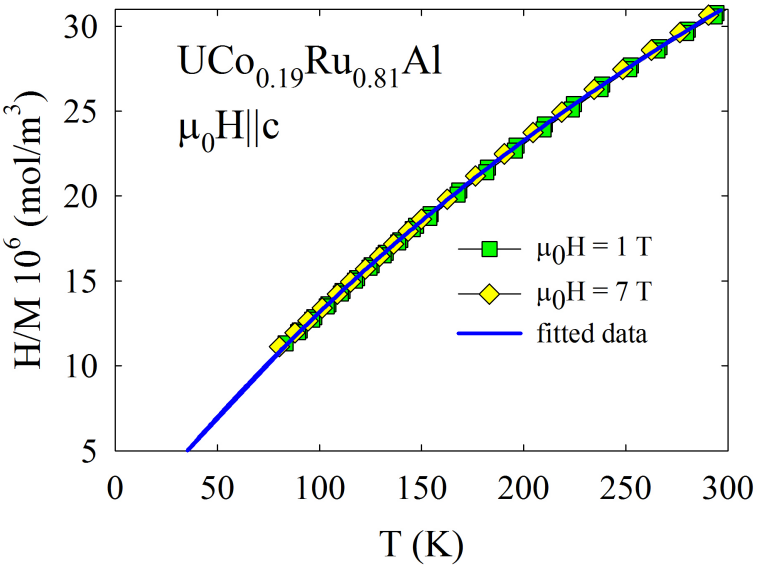

Figure 5.25: Temperature dependence of inverse susceptibility of $UCo_{0.19}Ru_{0.81}Al$ compound in various external magnetic fields applied along the c-axis.

5.5.2 Resistivity measurements

Samples from magnetization measurement were used for resistivity measurement. The resistivity for current applied along the a-axis shows almost no change down to low temperatures (Figure 5.26). Determined electrical resistivity at 300 K for current applied along a-axis is $\rho = 2.56\ 10^{-5}\ \Omega \cdot \mathrm{m}$. The resistivity for the c-axis behaves like T^x, where x = 1.49. The value of exponent can sign existence of quantum criticality [45].

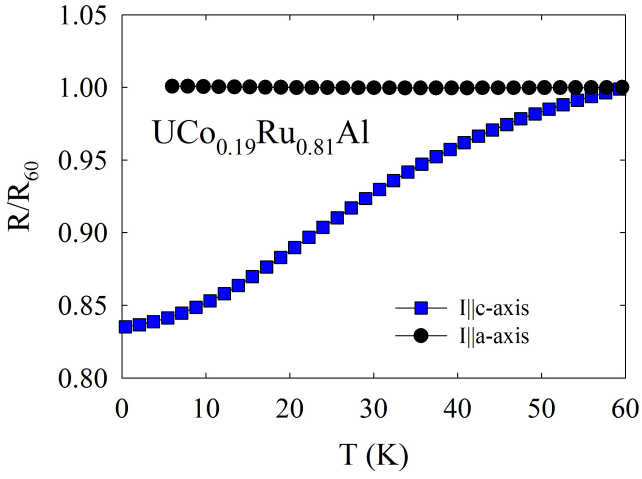

Figure 5.26: Temperature dependence of electrical resistivity $UCo_{0.19}Ru_{081}Al$ for current applied along the c-axis and a-axis.

5.5.3 Heat capacity measurements

Heat capacity was measured on sample of mass of 1.71 mg. Heat capacity data show sign of phase transition at 33 K which did not disappears in applied external magnetic field up to 14 T (Figure 5.27). The zero effect of the external magnetic field up to 14 T on the anomaly can suggest existence of structural phase transition, but such type of transition is not expected and we suppose only artefact effect of the measurement. Magnetic part of the heat capacity divided by temperature shows sign of non-Fermi liquid behaviour (Figure 6.8). Coefficient γ had been determined $\gamma = 63.9\ \mathrm{mJ/mol \cdot K^2}$.

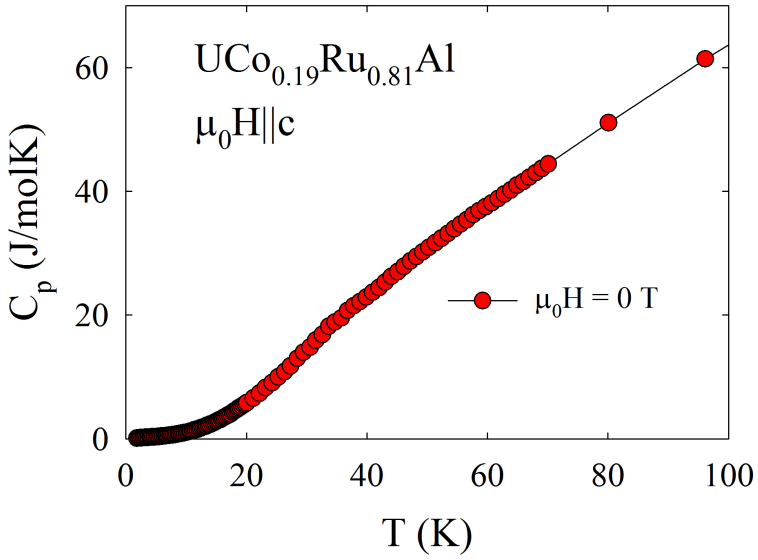

Figure 5.27: Temperature dependence of heat capacity of $UCo_{0.19}Ru_{0.81}Al$ compound.

6. Discussion

Concentrations of grown single crystals determined by EDX analysis are close to our intended single crystal concentrations as is shown in Figure 6.1. Expected effect of intended concentration should be still observable.

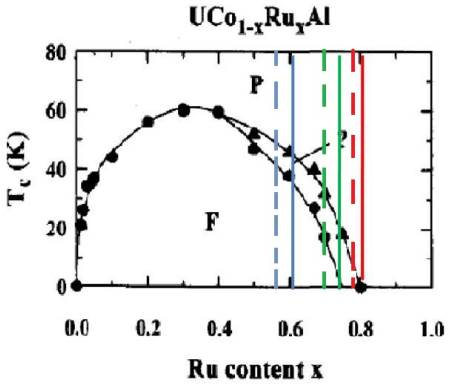

Figure 6.1: Concentration dependence of Curie temperature of $UCo_{1-x}Ru_xAl$ system. Full lines shows intended concentration of single crystals and interrupted lines show concentrations determined by EDX analysis.

Figure 6.2 shows hysteresis loops of $UCo_{0.40}Ru_{0.60}Al$, $UCo_{0.27}Ru_{0.73}Al$ and $UCo_{0.19}Ru_{0.81}Al$ together at the lowest measured temperatures. The saturated magnetic moment evidently decreasing with increasing Ru content and also shape of the loops has clear trend. While $UCo_{0.19}Ru_{0.81}Al$ has behaviour typical for a paramagnet, both loops of $UCo_{0.27}Ru_{0.73}Al$ and $UCo_{0.40}Ru_{0.60}Al$ compound behave ferromagnetically, when S-like shape cross to almost rectangular shape for $UCo_{0.40}Ru_{0.60}Al$. The results well correspond with phase diagram when the $UCo_{0.40}Ru_{0.60}Al$ should behave like hard ferromagnet. Nevertheless the shape of the loop of the $UCo_{0.27}Ru_{0.73}Al$ crystal is not far from the rectangular shape, as well. We cannot exclude presence of hard phase with respect to chemical analysis data which shifted our crystal to the left in the phase diagram. The birth of the magnetically hard phase can be presented in the lowest temperatures.

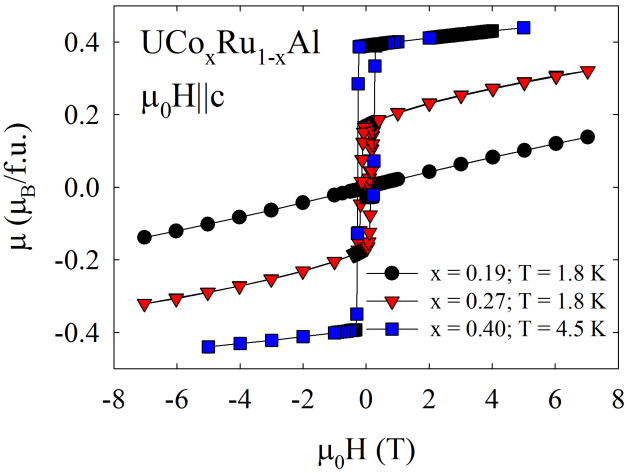

Figure 6.2: Hysteresis loops of $UCo_xRu_{1-x}Al$ for x = 0.40, x = 0.27 and x = 0.19.

Figure 6.3 shows temperature dependence of AC susceptibility of all crystals. The AC susceptibility data for $UCo_{0.40}Ru_{0.60}Al$ shows two anomalies which correspond to phase transitions as expected. The first phase transition from paramagnetic phase to the soft ferromagnetic one is at $T_C = 41$ K and the second one from soft ferromagnetic state to hard ferromagnetic one at 35 K. The anomaly in AC magnetic susceptibility data of $UCo_{0.27}Ru_{0.73}Al$ has maximum at 17.5 K which corresponds to phase transition from paramagnetic phase to soft ferromagnetic one. The width of anomaly suggests existence of other phase transition at temperature range between 5 - 10 K. Existence of the second anomaly can be explained by position of our crystal in the phase diagram. AC magnetic susceptibility data for $UCo_{0.19}Ru_{0.81}Al$ shows no anomaly down to lowest temperatures which is expected for a paramagnet.

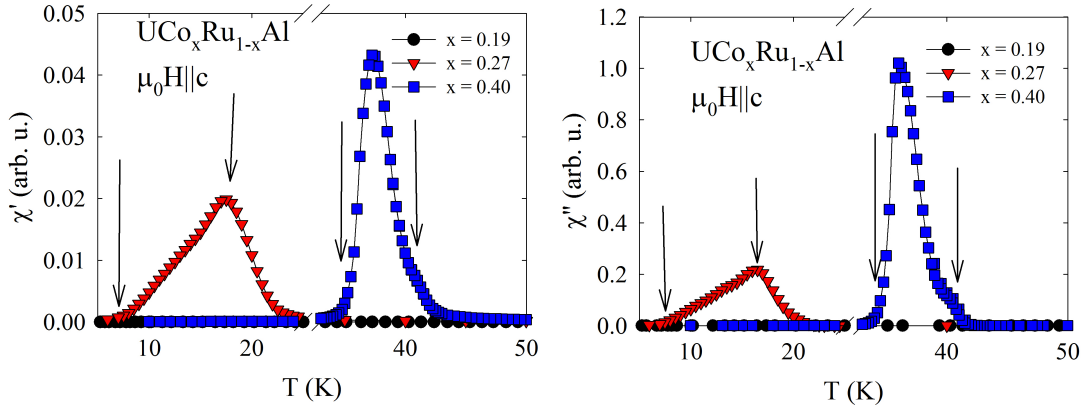

Figure 6.3: Temperature dependence of AC susceptibility of $UCo_xRu_{1-x}Al$ compounds for x = 0.4, x = 0.27 and x = 0.19.

The comparison of temperature dependence of magnetizations for all single crystals in Figure 6.4 shows rapid increase of magnetization (spontaneous magnetization). The found values are $\mu_{spont,0.40} = 0.44\ \mu_B$/f.u. and $\mu_{spont,0.27} =$

0.17 μ_B/f.u.. The spontaneous magnetic moment for $UCo_{0.40}Ru_{0.60}Al$ is 2.6 times bigger than for $UCo_{0.27}Ru_{0.73}Al$. Not only the temperature dependence of magnetization are different for all compounds. Fits of temperature dependencies of inverse magnetic susceptibility by modified Curie-Weiss law are shown in Figure 6.5. The Curie paramagnetic temperature from modified Curie-Weiss law for $UCo_{0.19}Ru_{0.81}Al$ is 1.2 K. This would mean existence of some ferromagnetic phase near this temperature but no effect in resistivity measurements was found which would confirm this.

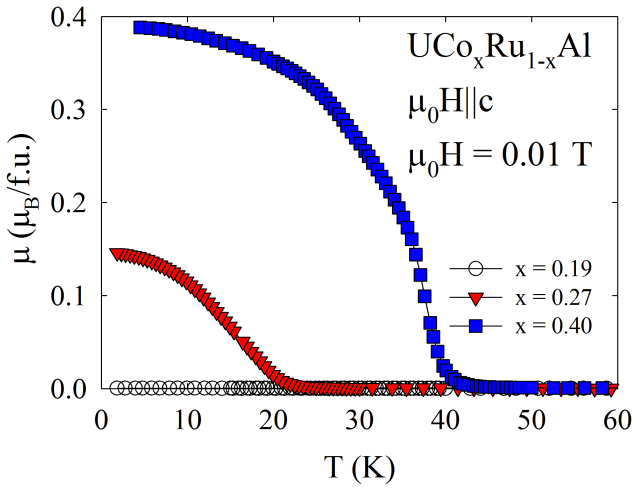

Figure 6.4: Temperature dependence of magnetization of $UCo_xRu_{1-x}Al$ compounds for x = 0.4, x = 0.27 and x = 0.19.

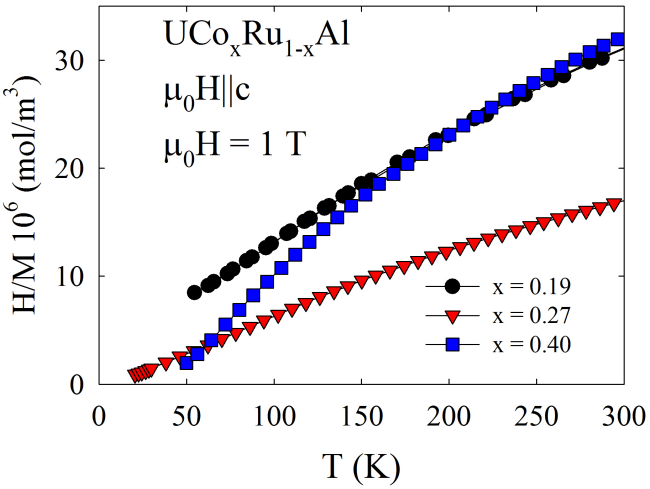

Figure 6.5: Temperature dependence of inverse magnetic susceptibility of $UCo_xRu_{1-x}Al$ for x = 0.4, x = 0.27 and x = 0.19.

Electrical resistivity for $UCo_{0.19}Ru_{0.81}Al$ has classical metallic-like character with no sign of any effect (Figure 6.6). Contrary to the first case, temperature dependence of electrical resistivity of $UCo_{0.27}Ru_{0.73}Al$ shows sudden rise at 20

K and the trend is conserved down to 0.4 K. This anomalous upturn is hardly suppressed by application of high external magnetic field along the c-axis as is shown in Figure 5.22. This is sign that the effect is of magnetic origin and not of structural one. Now we do not have any reliable explanation of this behaviour on the basis of performed macroscopic studies. Finally $UCo_{0.40}Ru_{0.60}Al$ shows first drop of resistivity at T = 41 K. Nevertheless not only one transition is detectable in this region. The second weak anomaly is found around 35 K. It is in good agreement with suggested phase diagram where cross between the magnetic phases is expected. We have also inspected the temperature trends of the resistivity data and we have found that $UCo_{0.40}Ru_{0.60}Al$ is characterized by T^2 trend typical for Fermi liquid behaviour while $UCo_{0.19}Ru_{0.81}Al$ represents T^x (x = 1.49) trend signing non-Fermi liquid features and possible presence of QCP.

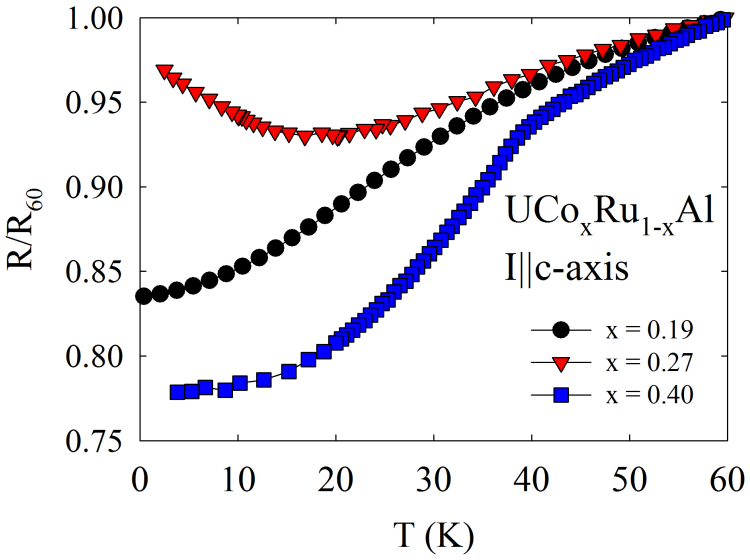

Figure 6.6: Temperature dependence of electrical resistivity of $UCo_xRu_{1-x}Al$ for x = 0.4, x = 0.27 and x = 0.19.

Heat capacity data of $UCo_xRu_{1-x}Al$ for x = 0.4, x = 0.27 and x = 0.19 are shown in Figure 6.7. No sign of anomaly was found in temperature dependence of the heat capacity data of $UCo_{0.27}Ru_{0.73}Al$ and $UCo_{0.19}Ru_{0.81}Al$. Such result is expectable for $UCo_{0.19}Ru_{0.81}Al$, but kind of anomaly was expected in the case of $UCo_{0.27}Ru_{0.73}Al$. We can conclude that the transition from the paramagnetic state to the soft ferromagnetic state is not visible because of itinerant character of the soft ferromagnetic phase (the change of magnetic part of entropy is zero) [1]. The other phase transition (potential transition to the hard phase) for $UCo_{0.27}Ru_{0.73}Al$ is not visible because of it is probably located in lower temperatures than were achieved. Same reason comes into force (zero entropy change for transition to soft ferromagnetic phase from paramagnetic phase) for detecting only one anomaly in $UCo_{0.40}Ru_{0.60}Al$ which corresponds to phase transition from soft ferromagnetic phase to hard one. The anomaly at temperature 35 K is suppressed by external magnetic field applied along the c-axis. Magnetic parts of heat capacity of $UCo_{0.27}Ru_{0.73}Al$ and $UCo_{0.19}Ru_{0.81}Al$ were determined using Debay model for $UCo_{0.40}Ru_{0.60}Al$ (Figure 6.8). Linearity of the temperature de-

pendence of magnetic heat capacity divided by temperature in logarithmic scale is sign of possible existence of non-Fermi liquid behaviour.

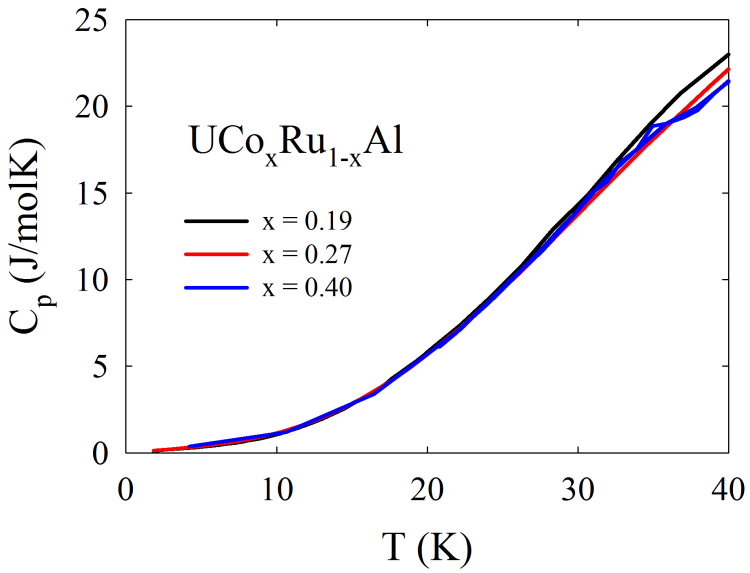

Figure 6.7: Temperature dependence of heat capacity of $UCo_xRu_{1-x}Al$ for x = 0.4, x = 0.27 and x = 0.19.

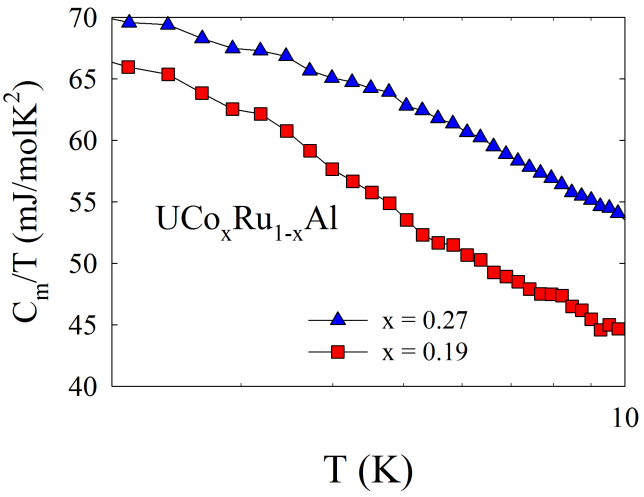

Figure 6.8: Magnetic part of heat capacity divided by temperature in logarithmic scale for $UCo_{0.19}Ru_{0.81}Al$ and $UCo_{0.27}Ru_{73}Al$.

7. Conclusions

The study of single crystals of the $UCo_{0.19}Ru_{0.81}Al$, $UCo_{0.27}Ru_{73}Al$ and $UCo_{0.40}Ru_{60}Al$ compounds confirmed that they all crystallize in the hexagonal ZrNiAl-type structure for all the three compounds. The crystals were investigated by measuring magnetization (magnetic susceptibility), heat capacity and electrical resistivity as functions of temperature and magnetic fields. For all three crystals we have found strong uniaxial anisotropy with the easy magnetization axis along the c-axis which is a common feature of all the isostructural UTX compounds.

Magnetization data confirm existence of two ferromagnetic phases - soft at higher temperatures and hard ground state phase (Figure 7.1), which were predicted by polycrystalline study [2]. The soft ferromagnetic phase seams to have entirely itinerant character as implied from missing anomaly of the heat capacity at T_C (no entropy change at T_C). We demonstrate the presence of the two magnetic phases in the $UCo_{0.40}Ru_{0.6}Al$ crystal in set of figures where are displayed all measured physical quantities (Figure 7.1). Two colour lines mark the critical temperatures. The evidence of both anomalies is not detectable in all quantities. The transition to the magnetically soft phase from paramagnetic state is detectable by AC susceptibility, DC magnetization and resistivity. Transition from the soft phase to the hard phase is in addition visible in specific heat data.

We have found a signs of proximity of a quantum critical point for $UCo_{0.19}Ru_{0.81}Al$ and $UCo_{0.27}Ru_{0.73}Al$ compounds. We suppose presence of QCP and non-Fermi liquid behaviour on the basis of evaluated critical parameters of temperature dependence of heat capacity and electrical resistivity. We expect sign of non-Fermi liquid behaviour from linearity of temperature dependence of magnetic heat capacity divided by temperature in logarithmic scale and non-integer value of the critical exponent of the temperature dependence of electrical resistivity, which were found in $UCo_{0.19}Ru_{0.81}Al$ and $UCo_{0.27}Ru_{73}Al$. The two ferromagnetic phases $UCo_{1-x}Ru_xAl$ compounds resemble situation in UGe_2 which is also characterized by two ferromagnetic phases and quantum critical point which is located between those two ferromagnetic phases and surprisingly, superconductivity appears there [4]. The unsolved question of our work is if only one quantum critical point with wide area of non-Fermi liquid behaviour is presented in $UCo_{1-x}Ru_xAl$ system or two different quantum critical points for each phase which are not fully separated. Both these scenarios will be subject of further research.

All important parameters of all compounds are summarized in Table 7.1.

Table 7.1: List of the parameters for $UCo_{0.19}Ru_{0.81}Al$, $UCo_{0.27}Ru_{73}Al$ and $UCo_{0.40}Ru_{60}Al$.

	$UCo_{0.19}Ru_{81}Al$	$UCo_{0.27}Ru_{73}Al$	$UCo_{0.40}Ru_{60}Al$
$T_{S\rightarrow H}$ [K] from HC	-	-	34.5
Θ_D [K]	-	-	189.7
γ [$mJ \cdot mol^{-1} \cdot K^{-2}$]	63.9	69.4	50.3
T_C [K] from ACT	-	-	41
$T_{S\rightarrow H}$ [K] from ACT	-	-	35
T_C [K] from AC	-	17.5	41
$T_{S\rightarrow H}$ [K] from AC	-	-	35
T_C [K] from M/T	-	18.7	41.3
$T_{S\rightarrow H}$ [K] from M/T	-	-	35.5
T_C [K] from Arrot	-	17.2	39.7
Θ_P [K]	1.2	19.1	42.6
μ_{eff} [μ_B]	2.03	2.67	1.78
μ_0 [$10^{-8} m^3 \cdot mol^{-1}$]	1.03	1.89	1.15
μ_{sat} [μ_B/f.u.]	-	0.32 (T = 1.8 K)	0.44 (T = 4.5 K)
μ_{spont} [μ_B/f.u.] (μ_0 H = 0.01 T)	0 (T = 1.8 K)	0.15 (T = 1.8 K)	0.39 (T = 4.5 K)

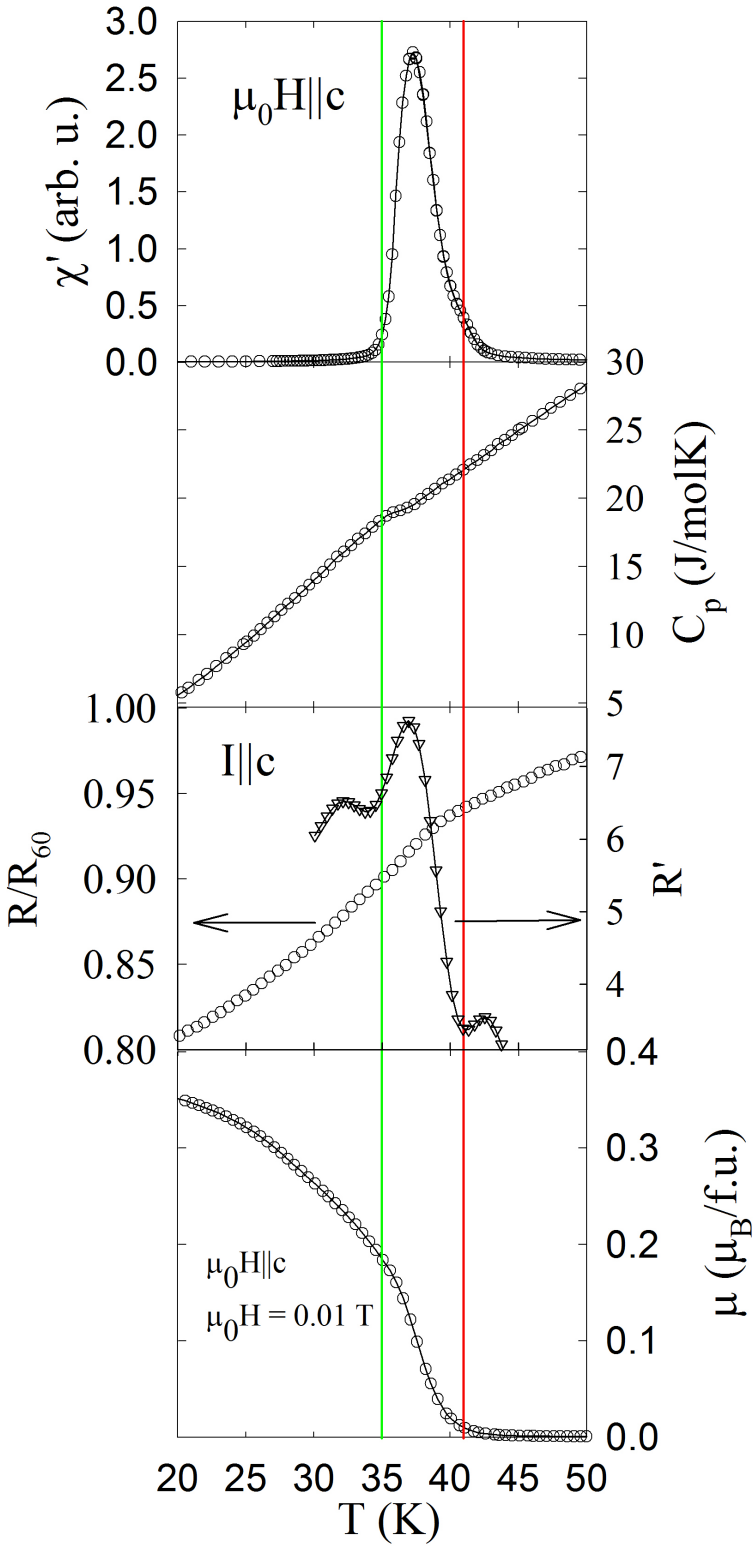

Figure 7.1: Phase transitions in $UCo_{0.40}Ru_{0.60}Al$. Red line represents phase transition between paramagnetic and soft ferromagnetic phase and green line represents transition between soft ferromagnetic phase and hard one.

8. Future plans

Pseudoternary $UCo_xRu_{1-x}Al$ system shows very interesting physical properties, which were studied only by macroscopic techniques available in our department, but detail information regarding the microscopic origin of the observed effects are still missing. Study of potential existence of quantum critical point or points and their properties is subject of future research. We have already applied to LLB for a polarized neutron diffraction experiment to investigate magnetic state of $UCo_{0.40}Ru_{60}Al$. Moreover we plan to submit a proposal to the spectrometer PANDA in FMR II for inelastic neutron study. We also have in mind to carry out measurements of bulk physical properties of the other two compounds under hydrostatic and uniaxial pressure and tune the magnetic state to quantum critical point by pressure.

References

[1] V. Sechovsky and L. Havela. *Chapter 1 Magnetism of ternary intermetallic compounds of uranium*, volume Volume 11, pages 1–289. Elsevier, 1998.

[2] A. V. Andreev, L. Havela, V. Sechovsky, M. I. Bartashevich, J. Sebek, R. V. Dremov, and I. K. Kozlovskaya. Ferromagnetism in the $UCo_{1-x}Ru_xAl$ quasiternary intermetallics. *Philosophical Magazine B-Physics of Condensed Matter Statistical Mechanics Electronic Optical and Magnetic Properties*, 75(6):827–844, 1997.

[3] R. Troc, V. H. Tran, F. G. Vagizov, I. M. Reznik, and L. Shlyk. Magnetism and chemical bonding in the systems $U(Fe_{1-x}T_x)Al$ (T = Co, Ni). *Physica B: Condensed Matter*, 199-200(0):647–650, 1994.

[4] A. Huxley, E. Ressouche, B. Grenier, D. Aoki, J. Flouquet, and C. Pfleiderer. The co-existence of superconductivity and ferromagnetism in actinide compounds. *Journal of Physics-Condensed Matter*, 15(28):S1945–S1955, 2003.

[5] S. Blundell. *Magnetism in Condensed Matter*. Oxfor University Press, Grear, 2001.

[6] T. Kasuya. A theory of metallic ferro- and antiferromagnetism on zener's model. *Progress of Theoretical Physics*, 16(1):45–57, 1956.

[7] M. A. Ruderman and C. Kittel. Indirect exchange coupling of nuclear magnetic moments by conduction electrons. *Phys. Rev.*, 96:99–102, 1954.

[8] K. Yosida. Magnetic properties of Cu-Mn alloys. *Phys. Rev.*, 106:893–898, 1957.

[9] P. Fulde and M. Loewenhaupt. Magnetic excitations in crystal-field split 4f systems. *Adv. Phys.*, 34(5):589–661, 1985.

[10] J. A. Hertz. Quantum critical phenomena. *Phys. Rev. B*, 14:1165–1184, Aug 1976.

[11] A. Beiser. *Concepts Of Modern Physics*. McGraw-Hill Education (India) Pvt Limited, 2002.

[12] S. Stolen and T. Grande. *Chemical Thermodynamics of Materials: Macroscopic and Microscopic Aspects*. Wiley, 2004.

[13] P. Svoboda, P. Javorsky, M. Divis, V. Sechovsky, F. Honda, G. Oomi, and A. A. Menovsky. Importance of anharmonic terms in the analysis of the specific heat of UNi_2Si_2. *Phys. Rev. B*, 63:212408, 2001.

[14] C. A. Martin. Simple treatment of anharmonic effects on the specific heat. *Journal of Physics: Condensed Matter*, 3(32):5967, 1991.

[15] P. Svoboda. *Komplexní přístup k analýze nízkoteplotního měrného tepla*. MFF UK Praha, 2006.

[16] N. W. Ashcroft and N. D. Mermin. *Solid state physics*. Science: Physics. Saunders College, 1976.

[17] J. Rodriguez-Carvajal. Recent advances in magnetic structure determination by neutron powder diffraction. *Physica B: Condensed Matter*, 192(1-2):55 – 69, 1993.

[18] http://www.tescan.com/.

[19] http://www.qdusa.com/.

[20] V. Sechovsky, L. Havela, F. R. de Boer, J. J. M. Franse, P. A. Veenhuizen, J. Sebek, J. Stehno, and A. V. Andreev. Systematics across the UTX series (T = Ru, Co, Ni; X = Al, Ga, Sn) of high-field and low-temperature properties of non-ferromagnetic compounds. *Physica B+C*, 142(3):283–293, 1986.

[21] F. R. de Boer, E. Bruck, A. A. Menovsky, P. A. Veenhuizen, V. Sechovsky, L. Havela, and K. H. J. Buschow. High-field magnetization of ternary uranium 1:1:1 intermetallics. *Physica B: Condensed Matter*, 155(1-3):221–224, 1989.

[22] P. A. Veenhuizen, F. R. de Boer, A. A. Menovsky, V. Sechovsky, and L. Havela. Magnetic-properties of URuAl and URhAl single-crystals. *Journal De Physique*, 49(C-8):485–486, 1988.

[23] M. Samsel-Czekala, E. Talik, and R. Troc. Electronic structure, magnetic, and electrical properties of single-crystalline magnetic fluctuator URuAl and comparison with reference systems. *Physical Review B*, 78(24), 2008.

[24] L. Havela, L. Neuzil, V. Sechovsky, A. V. Andreev, C. Schmitzer, and G. Hilscher. Magnetic properties of UXCo X=Sn, Al, Ga. *Journal of Magnetism and Magnetic Materials*, 54-57, Part 1(0):551–552, 1986.

[25] L. Havela, A. V. Andreev, V. Sechovsky, I. K. Kozlovskaya, K. Prokes, P. Javorsky, M. I. Bartashevich, T. Goto, and K. Kamishima. 5f-band metamagnetism in UCoAl. *Physica B: Condensed Matter*, 230-232(0):98–101, 1997.

[26] A. V. Andreev, I. K. Kozlovskaya, N. V. Mushnikov, T. Goto, V. Sechovsky, L. Havela, Y. Homma, and Y. Shiokawa. Ferromagnetism in the $U_{1-x}Y_xCoRuAl$ system. *Journal of Magnetism and Magnetic Materials*, 196-197(0):658–659, 1999.

[27] A. V. Andreev, L. Havela, V. Sechovsy, M. I. Bartashevich, T. Goto, and K. Kamishima. 5f band metamagnetism in UCoAl: Effects of alloying and pressure. *Journal of Magnetism and Magnetic Materials*, 169(3):229–239, 1997.

[28] N. V. Mushnikov, T. Goto, A. V. Andreev, H. Yamada, and V. Sechovsky. Physics of anisotropic itinerant 5f-electron metamagnetism in $UCo_{1-x}T_xAl$ (T=Fe, Ni). *Journal of Magnetism and Magnetic Materials*, 272-276, Supplement(0):E207–E213, 2004.

[29] A. V. Andreev, I. K. Kozlovskaya, N. V. Mushnikov, T. Goto, V. Sechovsky, Y. Homma, and Y. Shiokawa. Magnetic properties of the $UCo_{1-x}T_xAl$ solid solutions (T=Rh and Ir). *Journal of Alloys and Compounds*, 284(1-2):77–81, 1999.

[30] H. Nakotte, F. R. de Boer, L. Havela, P. Svoboda, V. Sechovsky, Y. Kergadallan, J. C. Spirlet, and J. Rebizant. Magnetic-anisotropy of UCoGa. *Journal of Applied Physics*, 73(10):6554–6556, 1993.

[31] A. Purwanto, R. A. Robinson, K. Prokes, H. Nakotte, F. R. de Boer, L. Havela, V. Sechovsky, N. C. Tuan, Y. Kergadallan, J. C. Spirlet, and J. Rebizant. Structure, transport and thermal-properties of UCoGa. *Journal of Applied Physics*, 76(10):7040–7042, 1994.

[32] L. Havela, V. Sechovsky, P. Nozar, E. Bruck, F. R. de Boer, J. C. P. Klaasse, A. A. Menovsky, J. M. Fournier, M. Wulff, E. Sugiura, M. Ono, M. Date, and A. Yamagishi. Antiferromagnetic correlations in UNiAl. *Physica B: Condensed Matter*, 163(1-3):313–316, 1990.

[33] L. Havela, V. Sechovsky, L. Jirman, F. R. de Boer, and E. Bruck. Magnetic transitions in UNiGa. *Journal of Applied Physics*, 69(8):4813–4815, 1991.

[34] V. Sechovsky, L. Havela, P. Svoboda, A. V. Andreev, P. Burlet, K. Prokes, H. Nakotte, F. R. de Boer, E. Bruk, R. A. Robinson, and H. Maletta. Magnetic phase diagram of UNiGa. *Journal of Magnetism and Magnetic Materials*, 140-144, Part 2(0):1379–1380, 1995.

[35] V. H. Tran and R. Troc. Magnetic and transport properties of the UTIn series (T = Rh, Pd and Pt). *Journal of Magnetism and Magnetic Materials*, 88(3):287–294, 1990.

[36] V. Sechovsky, L. Havela, H. Nakotte, K. Prokes, E. Bruk, F. R. de Boer, K. H. J. Buschow, and A. V. Andreev. Magnetism and hybridization in UTIn compounds (T = Rh, Pt, Pd). *Journal of Magnetism and Magnetic Materials*, 140-144, Part 2(0):1391–1392, 1995.

[37] V. H. Tran and R. Troc. On magnetic transitions in a novel compound, UPdGa. *Journal of the Less Common Metals*, 175(2):267–270, 1991.

[38] V. H. Tran, G. Andreev, F. Bouree, R. Troc, and H. Noel. Ac-susceptibility and neutron diffraction studies of the $URu_{1-x}Pd_xGa$ system. *Journal of Alloys and Compounds*, 271-273(0):503–507, 1998.

[39] V. H. Tran and R. Troc. Magnetic and transport properties of the UTSn series (T = Co, Ni, Ru, Rh, Pd, Ir and Pt). *Journal of Magnetism and Magnetic Materials*, 102(1-2):74–86, 1991.

[40] T. T. M. Palstra, G. J. Nieuwenhuys, R. F. M. Vlastuin, J. van den Berg, J. A. Mydosh, and K. H. J. Buschow. Magnetic and electrical properties of several equiatomic ternary U-compounds. *Journal of Magnetism and Magnetic Materials*, 67(3):331–342, 1987.

[41] V. H. Tran, R. Troc, and D. Badurski. Transport properties of the ferromagnets UCoSn, URuSn, URhSn and UIrSn. *Journal of Alloys and Compounds*, 219(1-2):285–289, 1995.

[42] R. Kruk, R. Kmiec, K. Latka, K. Tomala, R. Troc, and V. H. Tran. Magnetic properties of UTSn compounds (T=Co, Rh, Ir, Ru) studied by Sn-119 mossbauer spectroscopy. *Physical Review B*, 55(9):5851–5857, 1997.

[43] F. Mirambet, B. Chevalier, L. Fournes, J. Ferreira da Silva, M. A. Frey Ramos, and T. Roisnel. On the physical behaviour of URhSn. *Journal of Magnetism and Magnetic Materials*, 140-144, Part 2(0):1387–1388, 1995.

[44] A. Arrott. Criterion for ferromagnetism from observations of magnetic isotherms. *Phys. Rev.*, 108:1394–1396, 1957.

[45] H. v Lohneysen. Fermi-liquid instability at magnetic-nonmagnetic quantum phase transitions. *Journal of Magnetism and Magnetic Materials*, 200(1-3):532 – 551, 1999.

List of Tables